

Icarus

A Mid-Infrared Study of Synthetic Glass and Crystal Mixtures Analog to the Geochemical Terranes on Mercury --Manuscript Draft--

Manuscript Number:			
Article Type:	Research paper		
Keywords:	Mercury, surface; Mineralogy; Infrared observations; Instrumentation; Spectroscopy		
Corresponding Author:	Andreas Morlok Institut für Planetologie Münster, Germany		
First Author:	Andreas Morlok		
Order of Authors:	Andreas Morlok Christian Renggli, Ph.D. Bernard Charlier, Ph.D. Olivier Namur, Ph.D. Stephan Klemme, Professor Maximilian P. Reitze, Dr. Iris Weber, Dr. Aleksandra N. Stojic, Dr. Karin E. Bauch Harald Hiesinger, Professor Jörn Helbert, Dr.		
Abstract:	<p>The MERTIS (MErcury Radiometer and Thermal Infrared Spectrometer) onboard of the BepiColombo ESA/JAXA mission to Mercury will map the surface of Mercury in the wavelength range of 7-14 μm and for the interpretation of these spectra a database of analog materials is needed. We analysed bulk grain size fractions of a series of analog materials relevant to the distinct terranes of Mercury in diffuse reflectance in the mid-infrared (2.5 μm to 18 μm). Mineral mixtures cover a wide range of modal amounts of forsterite, enstatite, diopside and plagioclase, the resulting spectra can be divided into three distinct groups: (1) is dominated by a single glass feature, (2) by forsterite bands, and (3) by pyroxene bands. Despite often high contents, plagioclase features, are usually 'overprinted' by forsterite and pyroxene bands.</p> <p>Spectral parameter CF, an easy obtainable proxy for chemistry (SiO_2) and polymerization (SCFM) places the hermean mixtures mostly in the intermediate and basaltic range. The correlation of parameters easily obtainable in remote sensing, Mg/Si ratio, and CF, allows differing materials from high-energy evaporation processes in impacts from such formed in igneous processes.</p> <p>Preliminary comparison with a spectrum covering most of the hermean surface shows some similarity with band positions of the Inter Crater Plain and Heavily Cratered Terrains (IcP-HCT) and High-Mg Northern Volcanic Plains (High-Mg NVP) mixtures, but none of our spectra is able to reproduce the remote sensing data entirely.</p>		
Suggested Reviewers:	Patrick Peplowski, Ph.D. Johns Hopkins University Patrick.Peplowski@jhuapl.edu Involved in MESSENGER mission, background in instrumentation	Karen Stockstill Cahill, Ph.D. Planetary Science Institute Karen.Stockstill-Cahill@jhuapl.edu Background in experimental petrology, infrared studies, and Mercury	Alessandro Pisello, Ph.D.

	<p>University of Perugia alessandro.pisello@unipg.it Works on glass and rocks in the mid-infrared</p>
	<p>Mehmet Yesiltas, Ph.D. Kırklareli University myesiltas@knights.ucf.edu Background in mid-infrared studies of extraterrestrial materials</p>
	<p>Timothy D. Glotch, Professor Stony Brook University timothy.glotch@stonybrook.edu Background in spectroscopy of rocks and minerals for remote planetary sensing.</p>
<p>Opposed Reviewers:</p>	

1 **A Mid-Infrared Study of Synthetic Glass and Crystal Mixtures Analog to the Geochemical Terranes on**
2 **Mercury**

3 Andreas Morlok¹ (Corresponding Author; morlokan@uni-muenster.de; ++49 251 33424)

4 Christian Renggli²

5 Bernard Charlier³

6 Olivier Namur⁴

7 Stephan Klemme²

8 Maximilian P. Reitze¹

9 Iris Weber¹

10 Aleksandra N. Stojic¹

11 Karin E. Bauch¹

12 Harald Hiesinger¹

13 Joern Helbert⁵

14 ¹Institut für Planetologie, Westfälische Wilhelms-Universität Universität Münster, Wilhelm-Klemm-
15 Straße 10, 48149, Germany

16 ²Institut für Mineralogie, Westfälische Wilhelms-Universität Universität Münster, Corrensstrasse 24,
17 48149 Münster

18 ³University of Liege, Department of Geology, 4000 Sart-Tilman, Belgium

19 ⁴Department of Earth and Environmental Sciences, KU Leuven, 3001 Leuven, Belgium

20 ⁵Institute for Planetary Research, DLR, Rutherfordstrasse 2, 12489 Berlin, Germany

21
22
23
24
25
26
27
28
29
30
31

32

Abstract

33 The MERTIS (MErcury Radiometer and Thermal Infrared Spectrometer) onboard of the BepiColombo
34 ESA/JAXA mission to Mercury will map the surface of Mercury in the wavelength range of 7-14 μm and
35 the interpretation of these spectra a database of analog materials is needed. We analysed bulk grain size
36 fractions of a series of analog materials relevant to the distinct terranes of Mercury in diffuse reflectance
37 in the mid-infrared (2.5 μm to 18 μm). Mineral mixtures cover a wide range of modal amounts of
38 forsterite, enstatite, diopside and plagioclase, the resulting spectra can be divided into three distinct
39 groups: (1) is dominated by a single glass feature, (2) by forsterite bands, and (3) by pyroxene bands.
40 Despite often high contents, plagioclase features, are usually 'overprinted' by forsterite and pyroxene
41 bands.

42 Spectral parameter CF, an easy obtainable proxy for chemistry (SiO_2) and polymerization (SCFM) places
43 the hermean mixtures mostly in the intermediate and basaltic range. The correlation of parameters
44 easily obtainable in remote sensing, Mg/Si ratio, and CF, allows differing materials from high-energy
45 evaporation processes in impacts from such formed in igneous processes.

46 Preliminary comparison with a spectrum covering most of the hermean surface shows some similarity
47 with band positions of the Inter Crater Plain and Heavily Cratered Terrains (IcP-HCT) and High-Mg
48 Northern Volcanic Plains (High-Mg NVP) mixtures, but none of our spectra is able to reproduce the
49 remote sensing data entirely.

50

51 **Key Words:** Mercury, surface; Mineralogy; Infrared observations; Instrumentation; Spectroscopy

52

53

54

55 **1. Introduction**

56 The mid-infrared spectrometer MERTIS (MErcury Radiometer and Thermal Infrared Spectrometer) of
57 BepiColombo will map the surface of Mercury in the wavelength range of 7-14 μm , with a spatial
58 resolution of around 500 meters (Hiesinger et al., 2020). Spectral infrared features permit the direct
59 determination of Mercury's surface mineralogy (e.g., Rothery et al., 2020), which is not possible with
60 ground-based observations at this resolution (e.g., Sprague et al., 2009). In order to extract a more
61 accurate, as well as spatially-resolved mineralogy from the future spectral data, laboratory studies for
62 comparison with BepiColombo measurements are required to support spectral modelling. In order to
63 achieve this, the IRIS laboratory in Münster and the BED laboratory in Berlin were installed to
64 characterize a wide range of samples relevant to Mercury (e.g. Weber et al. 2018).

65 There are no known meteorites from Mercury (e.g., Weber et al., 2016). Hence, we rely on
66 remote sensing observations to study the mineralogy of Mercury. Multispectral imaging with the
67 Mercury Dual Imaging System (MDIS) and spectral reflectance measurements with the Mercury
68 Atmospheric and Surface Composition Spectrometer (MASCS) onboard MESSENGER recognized the
69 occurrence of graphite (Peplowski et al., 2016), sulphides (Vilas et al., 2016), and ice in polar regions
70 (Neumann et al. 2013). Spectral measurements also show that the crust of Mercury contains Fe²⁺-poor
71 silicate minerals (Izenberg et al., 2014). However, spectral data from MESSENGER were insufficient to
72 identify the mineralogy of silicate phases and their abundances. Additionally, information on the
73 chemical composition of the hermean surface is based on data from X-ray, gamma-ray, and neutron
74 spectrometers onboard the MESSENGER spacecraft (e.g., Peplowski et al., 2011, 2016; Nittler et al.,
75 2020). Major element ratios obtained from the various instruments allowed the identification of several
76 chemically different regions (the so-called 'terranes') on the hermean surface. The terranes were named
77 the Low-Mg Northern Volcanic Plains (Low-Mg NVP), the High-Mg Northern Volcanic Plains (High-Mg

78 NVP), the Smooth Plains, the Inter Crater Plains and Heavily Cratered Terrains (IcP-HCT), and the High-
79 Mg Province (Nittler et al., 2011; Peplowski et al., 2016; Weider et al., 2015; vander Kaaden et al., 2016;
80 Peplowski and Stockstill-Cahill, 2019). Typical rock types on Mercury's surface can broadly be described
81 as Fe-free and S-enriched komatiites, boninites, and andesites (e.g., Weider et al., 2015; Vander Kaaden
82 et al., 2016; Peplowski and Stockstill-Cahill, 2019). Thermodynamic modeling and experimental petrology
83 provide first order constraints on the mineralogy of such rocks, which are likely to be dominated by
84 olivine, pyroxenes, plagioclase \pm quartz, and (Mg,Ca)S sulfide (e.g., Charlier et al., 2013, Stockstill-Cahill
85 et al., 2012; Namur & Charlier 2017; Vander Kaaden et al., 2017; Renggli et al., 2022). Data from mid-
86 infrared spectroscopy from terrestrial telescopic observations integrating large surface regions also
87 indicate a hermean mineralogy dominated by plagioclase and pyroxene (Donaldson-Hanna et al., 2007;
88 Sprague et al., 1994, 2000, 2002, 2007; Sprague and Roush, 1998; Emery et al., 1998; Cooper et al.,
89 2001).

90 In this study, we performed spectroscopic measurements in the mid-infrared wavelength range
91 of analog glass and crystal mixtures relevant to Mercury's surface. The compositions of the glasses and
92 crystals were chosen based on results from high-temperature crystallization experiments (1480-1100°C),
93 that were equilibrated at crustal pressure (1 kbar) and reduced redox conditions (around IW-5; Namur
94 and Charlier, 2017). The bulk compositions of these experiments are representative of the five main
95 chemically distinct regions of the hermean surface introduced above, and the quenched products
96 contain some of the following phases: silicate glass, plagioclase, forsterite, diopside, enstatite, quartz,
97 FeSi metal, and sulfide (i.e., stoichiometric FeS). The samples we measured in this study are mixtures of
98 pure endmember minerals and glass, very similar to the chemical compositions of the experimental
99 products presented by Namur and Charlier, 2017. Synthetic glasses used in this study were previously
100 described in detail in Morlok et al. (2021).

101 The overall aim of this study is to (a) provide mid-infrared reflectance spectra of hermean
 102 mineral/glass mixtures in different size fractions to allow granulometric studies, and under varying
 103 observational geometries to accommodate for changing observational conditions in orbit, and (b)
 104 provide first spectral parameters for the comparison with future data obtained by MERTIS.

105

ID	mineral / features	locality (origin)
13	Quartz	Mongolia
22	Diopside	Otter Lake, Quebec, Canada
28	Labradorite	Ihosy, Madagascar
53	Enstatite	Odegardens Verk, Bamble, Norway
249	Olivine	Dreiser Weiher, Germany

106 **Table 1:** Sources of natural crystalline phases used in this study. Samples are from larger,
 107 crushed single crystals and handpicked afterwards. Spectra can be found in Figure 2f. Chemical
 108 data see Table 3.

109

110 2. Samples and Techniques

111 2.1. Samples

112 Compositional and mineralogical characteristics of five terranes are covered in this study (Peplowski et
 113 al., 2015, Weider et al., 2015; Namur and Charlier, 2017; Denevi et al., Nittler et al., 2020). Large lava
 114 flows (~3.5 Ga) are typical of the Northern Volcanic Plains (Low-Mg and High-Mg NVP). The Low-Mg NVP
 115 is characterized by low Mg/Si ratios and a wider range of Al contents. This results in high-plagioclase
 116 abundance, together with diopside and forsterite, whereas the High-Mg NVP lavas contain a in
 117 comparison higher olivine abundance.

118 The intermediate Inter Crater Plain and Heavily Cratered Terrains (IcP-HCT), characterized by medium
119 sized craters, show high Al contents, and contrasting low Mg. This resulted in high modal amounts of
120 plagioclase.

121 3.5 to 3.9 Ga old Smooth plains cover ~40% of the hermean surface and are characterized by flat plains
122 with numerous wrinkle ridges. The chemistry shows lower Mg/Si, S/Si, and Ca/Si ratios compared to the
123 other regions, resulting in a mineralogy dominated by plagioclase, but minor mafic components. The old
124 (4.2 – 4 Ga) High-Mg Province is characterized by high Mg/Si and Ca/Si, and low Al/Si ratios. The samples
125 used in this study reflect a relatively low a a series of natural crystalline materials (Table 1). We selected
126 a series of modal (wt%) phase compositions for each surface region identified in Namur and Charlier
127 (2017) (Fig. 1). Chemical bulk compositions of the mixtures were calculated using the chemical
128 composition of the starting materials and the individual weighed phase abundances (Table 2).

129 Detailed information about the minerals labradorite, enstatite, and forsterite (IDs 28, 53, 249) used in
130 this study are given in Weber et al. (2021) and Reitze et al. (2021). ID 22 is a diopside, crushed to grain
131 sizes from 25 μm – 250 μm which shows no sign of impurity. However, in the grain size fraction from 0
132 μm – 25 μm we observe signs (<5%) of serpentinization (van der Meer et al., 1995; Daly et al., 2011).
133 However, this has only small impact on the overall bulk compositions of our samples because we used
134 low proportions of ID 22 Diopside in the mixtures.

135 The mineral samples are natural terrestrial materials. While the chemical composition of these minerals
136 is, overall, similar to minerals on Mercury, these phases formed in vastly different environments. In
137 particular, terrestrial magmatism is much more oxidized than expected for Mercury, with the latter of
138 which is characterized by redox conditions buffered by the iron-wüstite buffer (IW-7 to IW-3), whereas
139 magmatism on the Earth usually happens at redox conditions between IW-2 to IW+8 (McCubbin et al.,
140 2012; Namur et al., 2016a,b; Cartier and Wood, 2019). As a result, for example different $\text{Fe}^{2+}/\text{Fe}^{3+}$ ratios
141 in olivine and pyroxene can be expected.

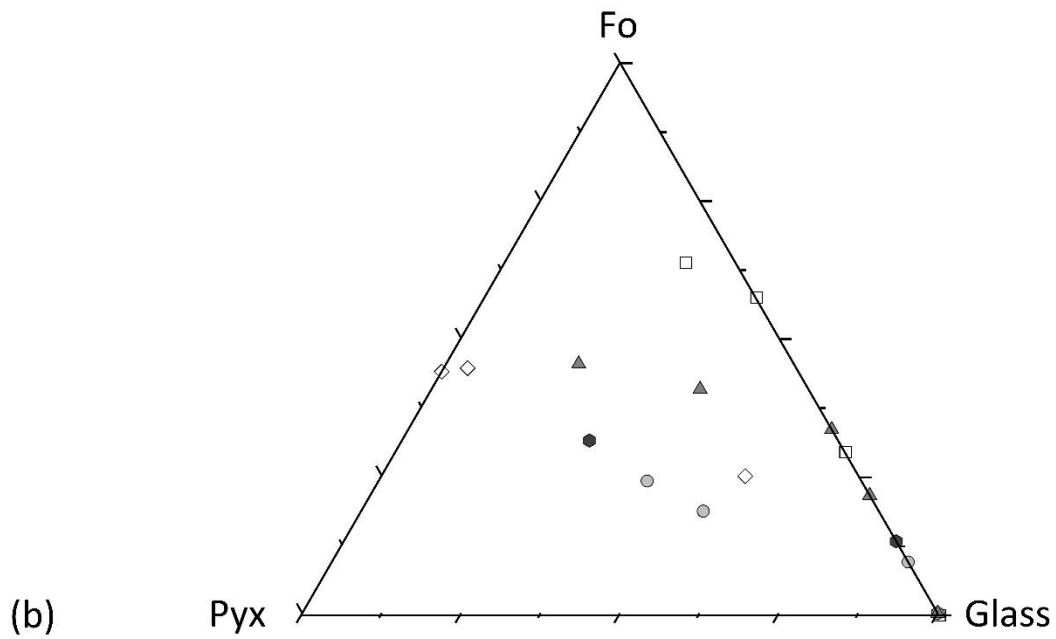
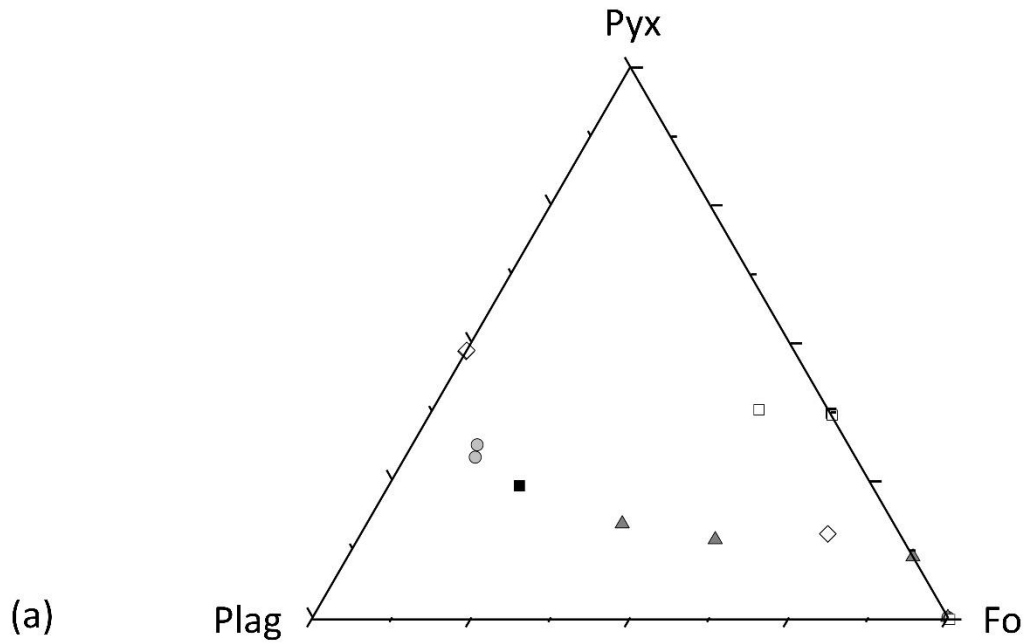
142 Silicate glasses were synthesized to represent the amorphous component in our mixtures. Details on the
143 synthesis protocol can be found in Morlok et al. (2021). We produced a series of six synthetic glasses
144 using reagent grade oxides as starting materials. Melts were kept in a gas mixing furnace for 6 h at
145 1450°C at the graphite-CO buffer (IW-6.7). The glasses cover the observed compositional range of the
146 terranes (e.g., 1.6 wt% - 19.0 wt% MgO).

147 Size fractions for each mixture were mixed separately (<25 µm, 25 µm – 63 µm, 63 µm -125 µm, 125 µm
148 -250 µm). This results in minor divergences from the modal starting compositions based on the
149 laboratory experiments (see Table 2). The finest fraction (<25 µm) was chosen to represent the regolith
150 grain size, which exhibits the important Transparency Feature (TF), a characteristic reflectance low. The
151 other size fractions were selected to cover intensity changes related with grain sizes. Increasing grain size
152 is correlated with increasing intensity (e.g., Salisbury, 1993; Mustard and Hayes, 1997).

153 For measurements, the samples were filled into aluminum sample cups, and the surface flattened with a
154 spatula (see Mustard and Hayes, 1997 for details).

155

156 **Figure 1:** Overview of the modal composition of the selected samples (Namur and Olivier, 2017). (a)
157 pyroxene, plagioclase, and forsterite, (b) pyroxene, forsterite, and glass. All in wt%.



- Smooth Plains (SP)
- High-Magnesium Province (High-Mg Province)
- ▲ Inter-Crater Plain and Heavily Cratered Plains (ICP-HcT)
- ◇ High Magnesium Northern Volcanic Plains (High-Mg NVP)
- Low Magnesium Northern Volcanic Plains (Low-Mg NVP)

Figure 1

159 2.2. Infrared Studies

160 We used a Bruker Vertex 70v infrared spectrometer with a liquid nitrogen cooled MCT (HgCdTe) detector
161 at the IRIS laboratory in Münster. Analyses were made in the wavelength region of 2.5 μm to 18 μm in
162 low vacuum (100 Pa). For each spectrum, 512 scans were accumulated at a spectral resolution of 4 cm^{-1}
163 (20 nm at 7 μm , 80 nm at 14 μm). This spectral resolution is comparable to MERTIS onboard
164 BepiColombo (e.g., 90 nm, Hiesinger et al. 2010 and 2020). For calibration, the instrument background
165 was eliminated by ratioing the sample spectra against the spectrum of a diffuse gold standard
166 (INFRAGOLD™) measured under the same conditions. Analyses were made at 13° incidence (i) and 13°
167 emergence (e), 20° (i)/30°(e), and 30°(i)/30°(e) in order to simulate observational geometries of an
168 orbiter. The results presented in the main text were made at 20°(i) and 30°(e), results for the other
169 settings are available in the supplement. The results are presented in reflectance from 6 μm – 18 μm
170 (Fig. 2a-e), which covers the range of the MERTIS instrument (7 μm – 14 μm) but omits volatile features.
171 It also includes the Christansen Feature (CF, the Reststrahlenbands RB; the molecular vibration modes of
172 the materials), and the Transparency Feature (TF; typical for the finest <25 μm size fractions).
173 Since the aim of our study is to compare the laboratory data with future remote sensing data,
174 measurements from the laboratory have to be recalculated from reflectance to emissivity using
175 Kirchhoff's law: $\epsilon = 1 - R$ (R = Reflectance, ϵ = Emission, Nicodemus, 1965). However, a prerequisite for
176 the validity of Kirchhoff's law is that the reflected light should be collected in all directions. In an ideal
177 case directional emissivity and directional hemispherical reflectance should be compared. However, we
178 used a bi-directional setup. Earlier studies showed that this approach mainly affects the reflectance
179 intensity, but not band positions. This must however be kept in mind when comparing the results in a
180 quantitative manner with emission data (Salisbury et al., 1991; Hapke, 1993; Thomson and Salisbury,
181 1993; Salisbury et al., 1994; Christensen et al., 2001). The spectra presented in this study are accessible
182 on our online database at the Institut für Planetologie in Münster (<http://bc-mertis-pi.uni-muenster.de/>).

	Low-Mg NVP		High-Mg NVP			Smooth Plains			IcP-HCT			
	ID349 (Y131)	ID 350 (Y172)	ID 355 (Y133)	ID 356 (Y143)	ID 357 (Y144)	ID 345 (Y140)	ID 344 (Y143)	ID 343 (Y144)	ID 351 (Y126)	ID 352 (Y131)	ID 353 (Y132)	ID 354 (Y146)
	_P											
Glass	86.9	29.5	96.8	42.0	30.2	90.7	53.8	42.3	78.6	66.6	42.3	20.6
Forsterite	8:2	14.3	3.2	12	10.7	9.3	5.1	5.9	21.4	29.7	32.5	31.5
Diopside	4.9	17.1		9.1	12.1		2.2	10.7		3.7	8.1	8.3
Enstatite				16.0	20.3		11.3	7.4				5.0
Plagioclase		39.1		20.8	26.6		27.6	33.7			17.1	33.4
Quartz												1.2
SiO2	64.52	59.35	58.71	59.01	60.41	62.10	61.34	59.76	54,85	59.00	55.73	55.72
TiO2	0.20	0.09	0.40	0.11	0.10	0.42	0.13	0.11	0,28	0.16	0.11	0.07
Al2O3	13.42	15.40	10.61	12.34	12.04	12.97	16.02	15.96	12,98	10.29	11.31	12.47
Cr2O3	0.00	0.01	0.00	0.01	0.01	0.00	0.01	0.01	0,01	0.01	0.02	0.02
FeO	0.97	1.79	0.32	2.80	3.20	0.82	1.63	1.56	1,89	2.70	3.03	3.42
MnO	0.10	0.06	0.17	0.07	0.05	0.16	0.07	0.07	0,08	0.10	0.09	0.06
MgO	9.03	10.57	19.99	14.86	14.68	12.83	9.20	9.22	20,56	18.74	19.78	19.28
CaO	6.25	8.89	6.94	6.91	6.41	6.18	6.53	8.63	5,64	4.79	6.27	5.95
Na2O	5.22	3.92	3.19	3.64	3.29	4.36	4.70	4.34	3,84	4.01	3.46	3.06
K2O	0.20	0.23	0.10	0.17	0.19	0.18	0.21	0.21	0,11	0.16	0.15	0.18
Total	99.91	100.31	100.43	99.93	100.39	100.02	99.85	99.86	100,24	99.97	99.94	100.24
	High-Mg Prov.		Crystal line			Glass						
	ID 348 (Y126)	ID 347 (Y131)	ID 346 (Y146)	ID 249 Forsterite	ID 22 Diopside	ID 53 Enstatite	ID 28 Plagioclase	ID 13 Quarz	ID339	ID 338	ID 181	ID 174
Glass	70.5	42.5	27.7						100	100	100	100
Forsterite	29.5	36.2	35.8	100								
Diopside		21.2	25.3		100							
Enstatite			1.3			100						
Plagioclase			7.7				100					
Quartz			2.0					100				
SiO2	53.87	55.14	56.74	40.96	55.08	57.48	55.63	101.42	58.62	55.90	59.29	64.26
TiO2	0.30	0.11	0.09	0.02	0.05	0.04	0.01	0.01	0.35	0.41	0.41	0.46
Al2O3	7.73	6.63	6.41	0.04	0.31	0.14	27.87	0.01	16.49	7.31	10.95	14.30
Cr2O3	0.01	0.02	0.02	0.04	0.01	0.01	0.02	0.01	0.00	0.00	0.00	0.00
FeO	2.51	3.67	3.90	8.38	2.63	9.09	0.10	0.01	0.13	0.10	0.05	0.05
MnO	0.16	0.11	0.09	0.11	0.14	0.04	0.01	0.01	0.08	0.25	0.17	0.16
MgO	28.30	23.87	23.25	50.50	16.80	33.16	0.01	0.00	12.43	26.94	19.00	8.97
CaO	5.07	7.82	7.71	0.09	25.10	0.21	10.32	0.00	7.15	7.15	7.16	6.81
Na2O	2.33	2.59	2.16	0.01	0.19	0.02	5.29	0.01	4.88	2.95	3.29	4.81
K2O	0.08	0.10	0.13	0.00	0.01	0.01	0.31	0.01	0.14	0.11	0.11	0.19
Total	100.35	100.06	100.51	100.14	100.30	100.21	99.57	101.50	100.27	101.11	100.44	100.01
				Fo#91	En#46	En#86	An#51					
					Wo#50							

185 **Table 2.** Chemical bulk compositions (wt. %) and modal mixtures used in this study. Bulk chemical
186 compositions of the mixtures used in this study (in wt.%) were calculated using the chemical
187 compositions of the components and the modal compositions. ID + Number: Sample ID used in the IRIS
188 database (see 2.2. Infrared Studies). Name of sample based on starting composition used following
189 Namur and Charlier (2017). Fo#: Forsterite content, En#: Enstatite content, An#: Anorthite content, Wo#:
190 Wollastonite content (mol.%).

191

192 **3. Results**

193 Most samples show spectral features at wavelengths shorter than 7 μm , usually at 2.7 μm – 3.0 μm ,
194 3.4 μm – 4 μm , and 5 μm – 7 μm . These are volatile features due to adsorption and absorption of
195 terrestrial water and unavoidable minor contaminations of the terrestrial minerals used for the mixtures.
196

197 **3.1. Low-Mg Northern Volcanic Plains**

198 The glassy end member is represented by low Mg sample ID 174 (Morlok et al., 2021), and has the CF at
199 7.9 μm , the TF at 11.8 μm , and a single RB at 9.6 μm . The spectrum of ID 350 has the CF between 7.8 μm
200 and 8.1 μm , with several pyroxene RB at 9.4 μm , 9.9 μm , 10.2 μm , 10.5 μm – 10.6 μm and 10.8 μm . The
201 TF is located at 11.3 μm – 11.5 μm (Tab.4; Fig.2a, f). The dominance of the glassy component results in a
202 simpler spectrum with few bands for ID 349: the CF is at 7.8 μm - 7.9 μm , the TF at 11.6 μm . The
203 strongest olivine RB is at 9.4 μm -9.5 μm , with minor features at 10.2 μm and 10.5 μm - 10.6 μm (Tab.4;
204 Fig.2a, f).

205

206

207

208

209 **3.2. High-Mg NVP**

210 The glass-rich samples ID 355 and pure glass ID 181 have the CF at 8 μm to 8.1 μm and the TF at 11.9 μm .
211 They have a strong RB at 9.7 μm to 9.8 μm , ID 355 also has weak olivine bands at 10.5 μm . Crystal-
212 bearing ID 356 and ID 357 show similar pyroxene band positions, although they are different in
213 intensities and band shapes. Their CF is between 7.8 μm and 8.2 μm (Table 4; Fig. 2b, f). Common
214 pyroxene RBs are at 9.4 μm -9.5 μm , 10.2 μm , 10.5 μm , 10.8 μm , and 11.3 μm . At longer wavelengths,
215 bands occur at 14.4 μm -14.5 μm , and 15.6 -15.8 μm . The TF is located at 11.4 μm .

216

217 **3.3 Intra Crater Plains - Heavily Cratered Terrane (IcP-HCT)**

218 The glass endmember, represented by high-Mg glass ID 181 (Morlok et al., 2021) has the CF at 8 μm to
219 8.1 μm , the TF at 11.9 μm , and a single RB at 9.8 μm . Similar to the High-Mg Province, the spectra of the
220 IcP-HCT region (ID 351, ID 352, ID 353, ID 354) are dominated by olivine features, reflecting the forsterite
221 modes ranging from 21 to 33 wt% (Table 4; Fig. 2c, f). The CF is located between 7.8 μm and 8.2 μm . The
222 strongest RBs are at 9.4 μm - 9.7 μm , 10.2 μm , 10.5 μm -10.6 μm , and 11.9 μm . The TF is again a broad
223 feature without distinct maximum. A dip at 7 μm is observed for diopside-rich samples ID 353 and ID
224 354.

225

226 **3.4. Smooth Plains**

227 Glass-dominated mixture ID 345 has a CF range from 7.9 to 8 μm , with an RB at 9.6 μm , 10.2 μm and
228 10.5-10.6 μm . The TF is located at 11.8 μm .

229 The-Smooth Plains samples ID 343 and ID 344 show generally similar pyroxene band positions (Table 4;
230 Fig. 2d, f) reflecting their similar bulk composition, but with ID 344 having more pronounced, 'sharper'
231 bands. The CF is between 7.8 μm and 8 μm for ID 343, and between 7.8 μm and 7.9 μm for ID 344.

232 Significant RBs are between 9.4 μm and 9.6 μm and at 9.9 μm , 10.2 μm , 10.5 μm , 10.8 μm and 11.4 μm .

233 The TF is located at 11.7 μm . Various minor spectral features are found at longer wavelengths, mainly
234 from 15.5 μm to 15.8 μm . The diopside-rich sample ID 343 shows a dip at 6.9 μm to 7 μm (or a small
235 feature at 7.3 μm) in the finest grain size fraction.

236

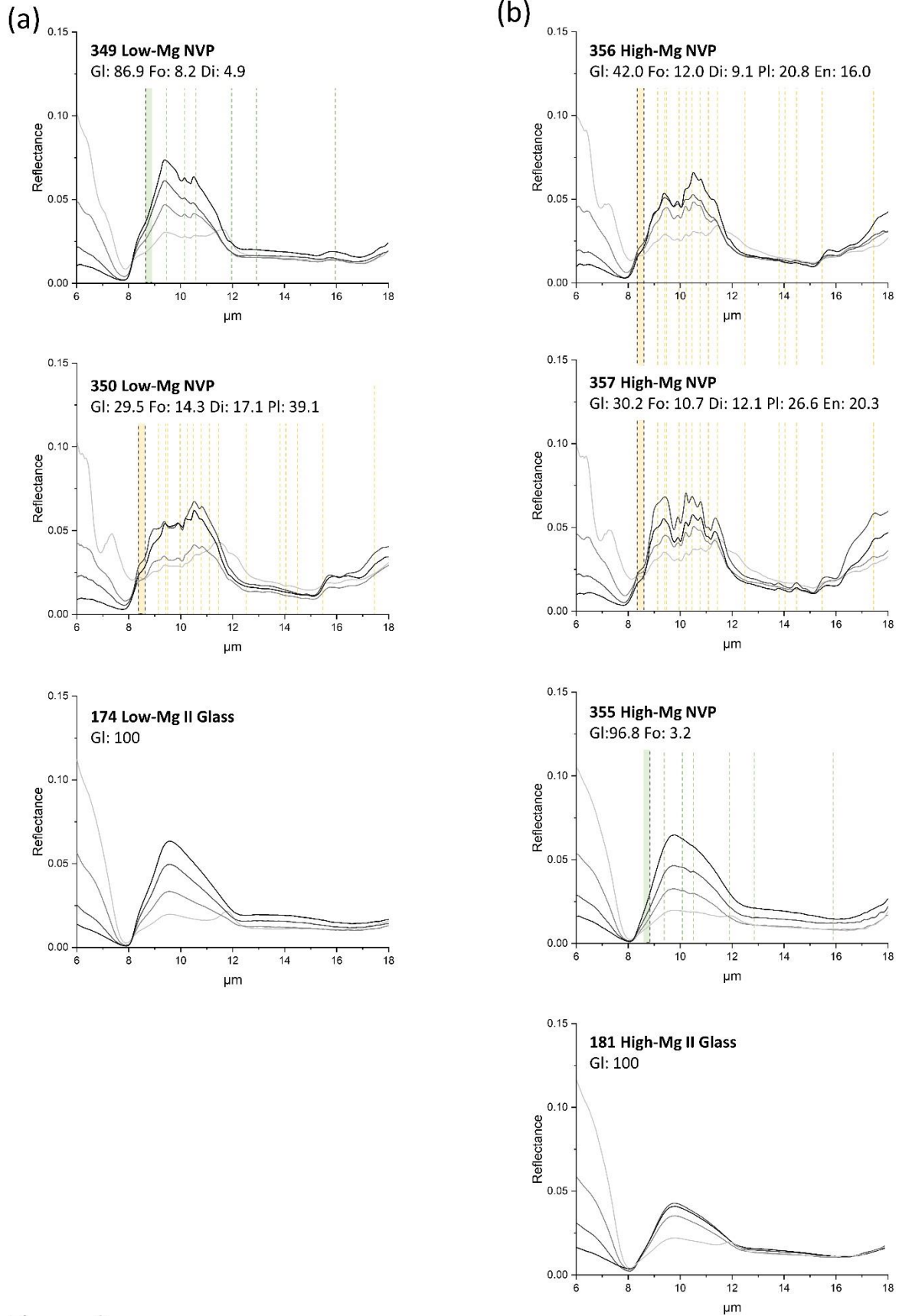
237 **3.5. High-Mg Province**

238 The glassy end member ID 338 has the CF at 8.2 μm , TF at 12.1 μm and the dominating RB at 9.9 μm .

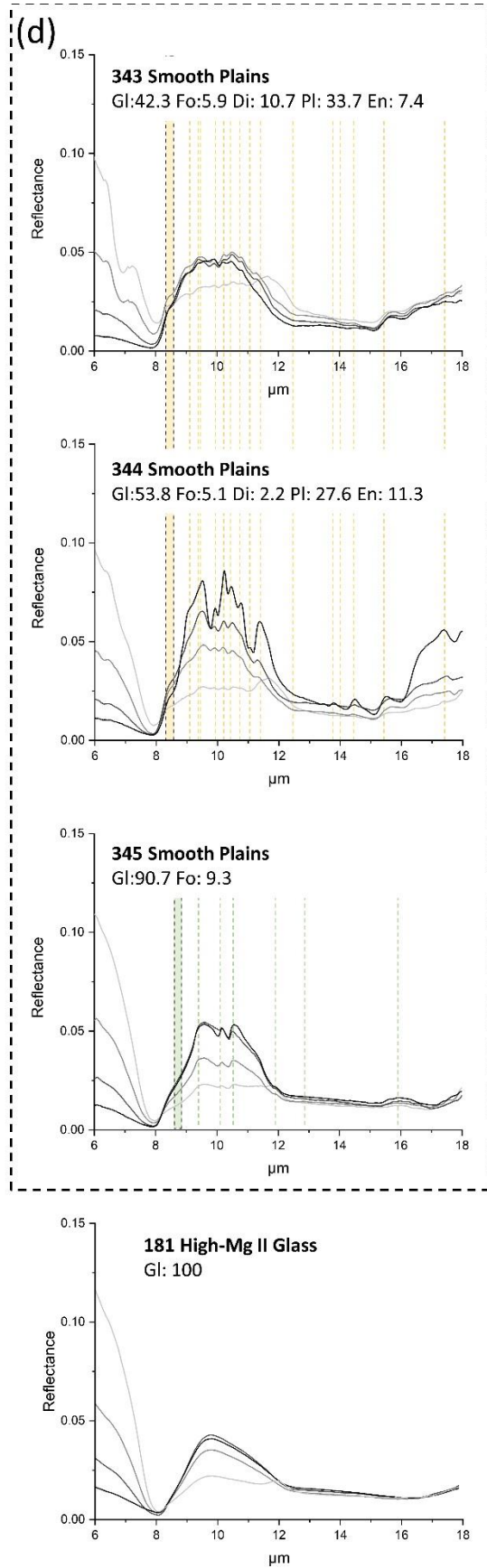
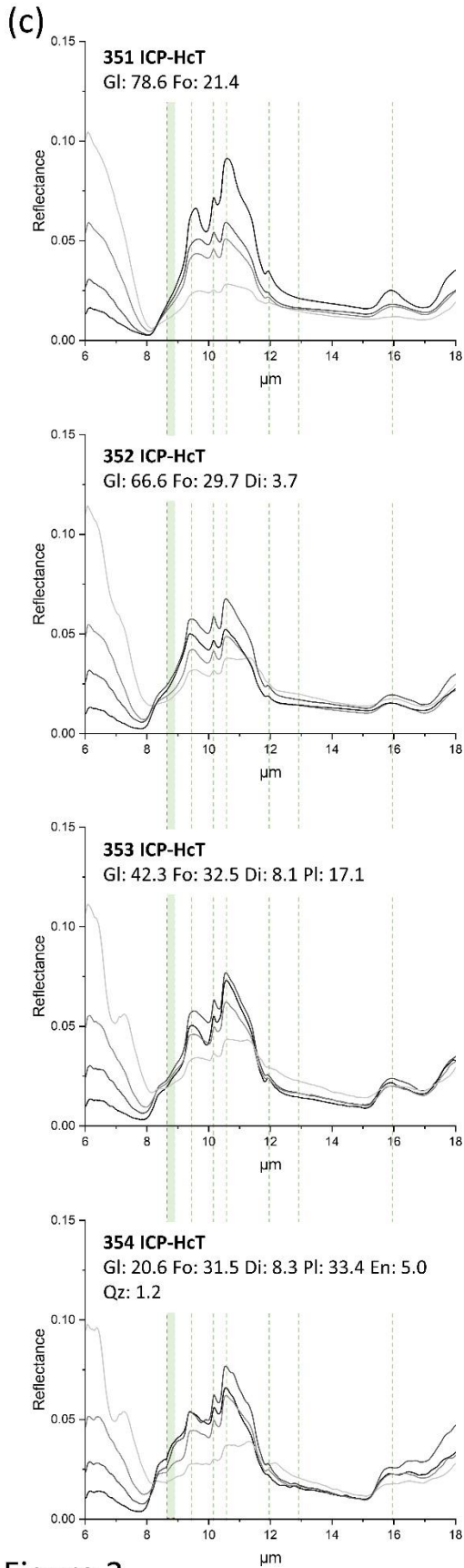
239 As a result of the high forsterite contents (30-36 wt%), spectra of mixtures ID 346, ID347, and ID348 are
240 quite similar (Table 2; Fig. 2e, f). The plagioclase and pyroxene contents show no significant bands in the
241 spectra. The CF ranges from 7.8 μm to 8.6 μm , and the strongest RB is at 10.6 μm . Further common
242 bands are found at 10.2 μm and 11.9 μm – 12 μm . ID 346 and ID 347 share further RBs at 9.4 μm and
243 10.8 μm . The TF is a broad feature without a clear peak. Features at longer wavelengths are seen
244 between 15.8 μm and 16 μm . Samples ID 346 and ID 347 shows a dip at 6.9 μm in the finest grain size
245 fractions.

246

247 **Figure 2a-f:** Mid-infrared reflectance spectra of the grain size fractions. Black: 125 - 250 μm , dark grey:
248 63 – 125 μm , grey: 25 - 63 μm , light grey: 0-25 μm . Gl: glass, Fo: forsterite, Di: diopside, Pl: plagioclase,
249 En: enstatite, Qz: quartz. Vertical green lines: 249 forsterite bands, vertical yellow lines: pyroxene
250 features (see Figure 3).



251 Figure 2



252 Figure 2

(e)

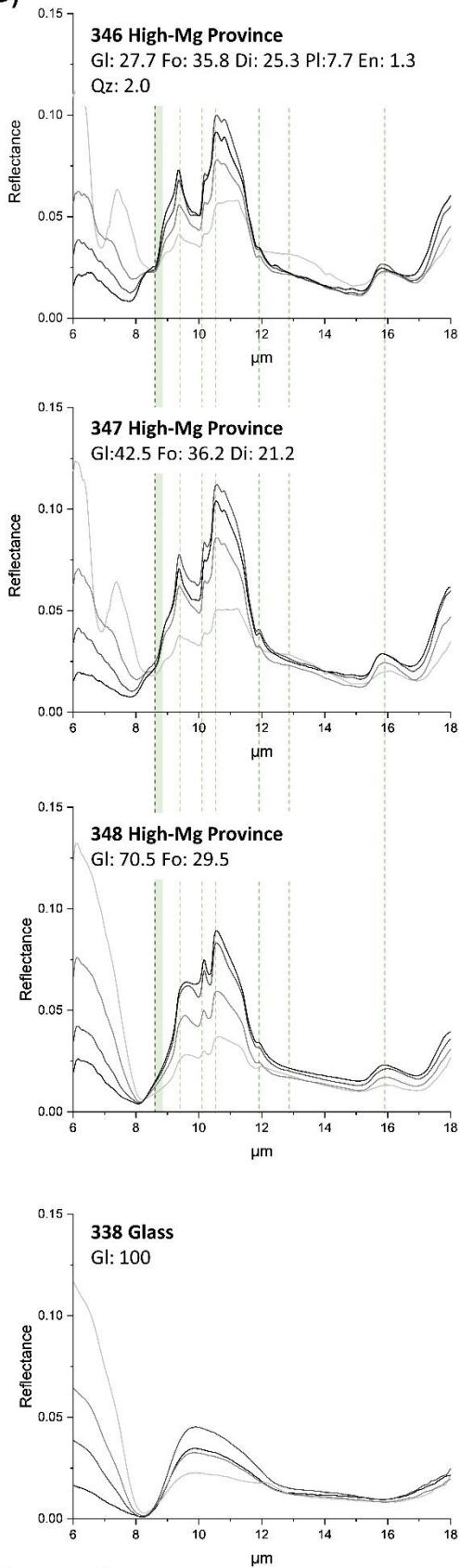
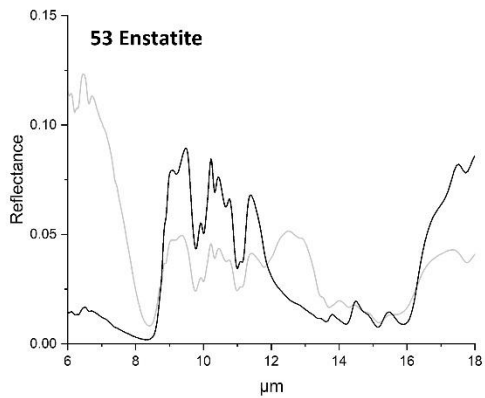
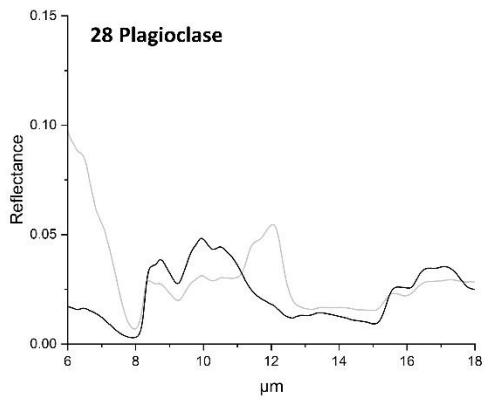
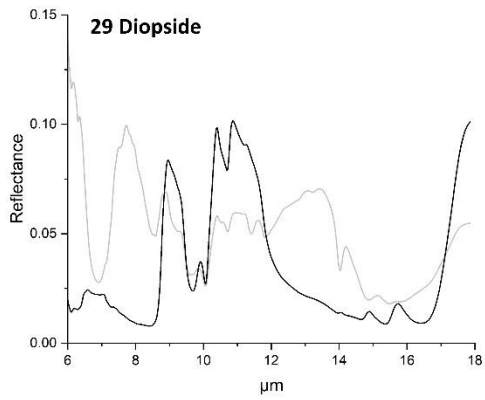
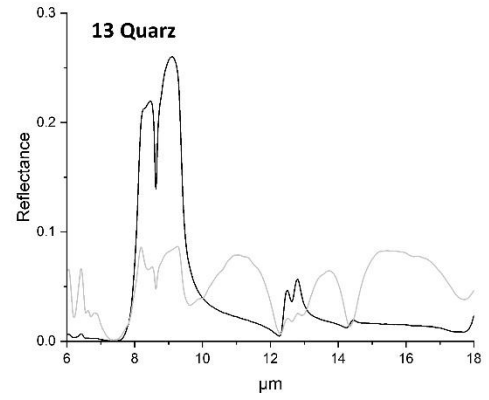
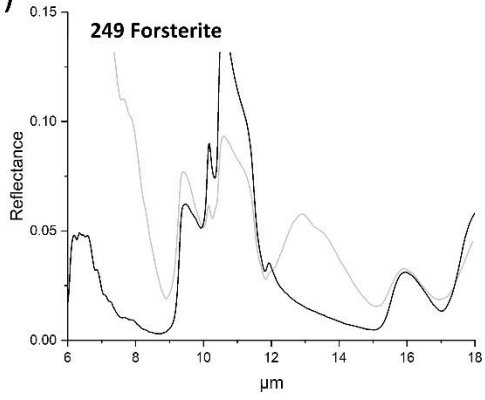


Figure 2

(f)



254 Figure 2

255 **4. Discussion**

256 **4.1. Interpreting the mixtures**

257 Despite the often-complex mixtures of up to five crystalline and one amorphous phase, the resulting
258 spectra of the mixtures can be divided into three groups (Table 3). The simplest spectra are dominated
259 by glass, demonstrated by prominent RB from 7.9 μm – 8.3 μm . Besides the ‘pure’ glassy end members
260 (ID 174, ID181, and ID 338), sample ID 355 High-Mg NVP with only minor (3 wt%) crystalline content
261 shows barely any recognizable additional bands (Fig. 2b). In the second group, forsterite features tend to
262 dominate (Table 3): bands near 9.4 μm to 9.5 μm , 10.2 μm , 10.6 μm , 11.9 μm , and 15.9 μm -16 μm
263 (Fig.2c, e). In the finest size fraction (< 25 μm), the TF the 10.6 μm band is turned into a broader feature
264 with another peak at 11.2 μm to 11.3 μm .

265 A third group exhibits the pyroxene RB features of diopside and enstatite near 8.9 μm to 9.1 μm , 9.4 μm
266 - 9.5 μm , 9.9 μm , 10.2 μm , 10.4 μm - 10.8 μm , 11 μm - 11.1 μm - 11.3 μm , and 11.4 μm to 11.6 μm
267 (Fig.2a-e). The finest grain size fractions of diopside-rich samples also show a dip at 6.9 μm to 7 μm ,
268 which is also prominent in the finest grain size fraction of the ID 22 diopside bulk material.

269 Although plagioclase feldspar is often a dominant component in the mixtures, its RB features tend to be
270 subdued by the forsterite and enstatite bands. The only RB, which is visible in all samples with a high
271 amount of plagioclase is its RB 1 as a shoulder at around 8.3 μm (e.g. 356 and 357 High-Mg NVP; Fig. 4b).
272 This is probably caused by its flat spectrum, that is dominated by a broad RB at 8.7 μm , and particular at
273 9.9 μm to 10 μm and 10.5 μm to 10.6 μm , which are superimposed by the more pronounced pyroxene
274 and olivine bands. However, further hints of significant plagioclase contents are higher intensities in the
275 \approx 10 μm to 10.5 μm range due to the strong plagioclase double-feature, which provides a generally broad
276 feature, which serves as some kind of underlying continuum, as observed in samples ID 350 and ID 356
277 (Fig.2a, b). In the wavelength range around 12 μm glasses and plagioclases have overlapping TF. In
278 earlier experiments using plagioclase (ID28) with varying degrees of Al-Si order (Reitze et al. 2021a)
279 plagioclases with low degree of Al-Si order show a single TF, such with a higher order a double peak or

280 peak with shoulder, as seen in the case of the plagioclase ID28 used in this study (e.g. 350 Low-Mg NVP
 281 or 357 High-Mg NVP; Fig.2a, b).

282 The quartz content is too low (few wt%) to produce any recognizable RB (e.g., 2 wt.% in ID 346, 1.2 wt.%
 283 in ID 354; Fig.4b and e). This raises the question of the ‘critical’ concentration (i.e. detection limit) of a
 284 phase to be recognizable in a mixture. In simple mixtures of glass and a crystalline phase, minute
 285 contents of 3 wt.% olivine in ID 355 High-Mg NVP(Fig.2b) provide just enough signal to identify the
 286 mineral with features at 10.5 μm and 11.9 μm (Table 4). Contents of 9.3 wt% olivine in ID 345 Smooth
 287 Plains (Fig.2d) are easily recognizable with bands at 9.6 μm , 10.2 μm , 10.6 μm , and 11.4 μm (Table 4).
 288 However, two minor components of 8.2 wt.% olivine and 4.2 wt.% diopside in ID 349 Low-Mg NVP
 289 (Fig.4a) only allow the clear identification of the olivine 9.4-9.5 μm , 10.2 μm , 10.5 μm -10.6 μm , and 11.6
 290 μm . Increasing number of phases will make the identification of a minute phase in the crowded range
 291 around 10 μm difficult. For the semi-quantitative identification of further components, rationing of
 292 spectral parameters could provide an alternative.

293

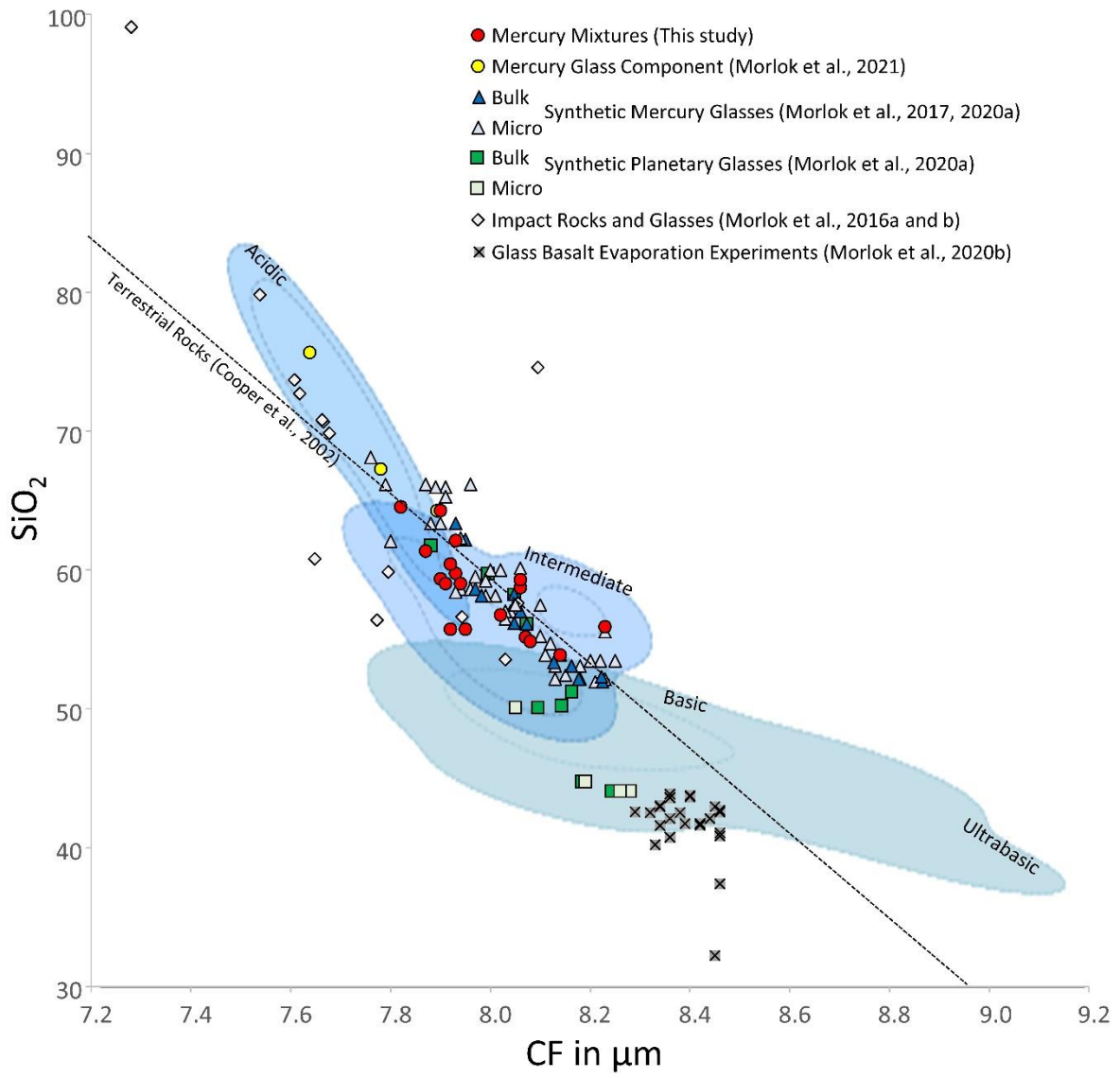
	RB Features	Samples
ID 338, 181,174 Glass	9.6 - 9.9 μm	ID 174, ID181, ID 338, ID 355 High-Mg NVP
ID 249 Forsterite	9.4 μm - 9.5 μm , 10.2 μm , 10.6 μm , 11.9 μm , 15.9 μm -16 μm	ID 349 Low-Mg NVP, ID 346, 347, 348 High-Mg Prov., ID 351, 352 353, 354 IcP-HCT, ID 345 Smooth Plains, ID 355 High-Mg NVP
ID53 Enstatite/ 29 Diopside	8.9 μm - 9.1 μm , 9.4 μm - 9.5 μm , 9.9 μm , 10.2 μm , 10.4 μm - 10.8 μm , 11 μm -11.1 μm - 11.3 μm , 11.4 μm to 11.6 μm	ID 350 Low-Mg NVP, ID 343, 344 Smooth Plains, ID 356, 357 High-Mg NVP

294 **Table 3.** Overview of the groups into which the mixture spectra can be divided based on their dominant
 295 features.

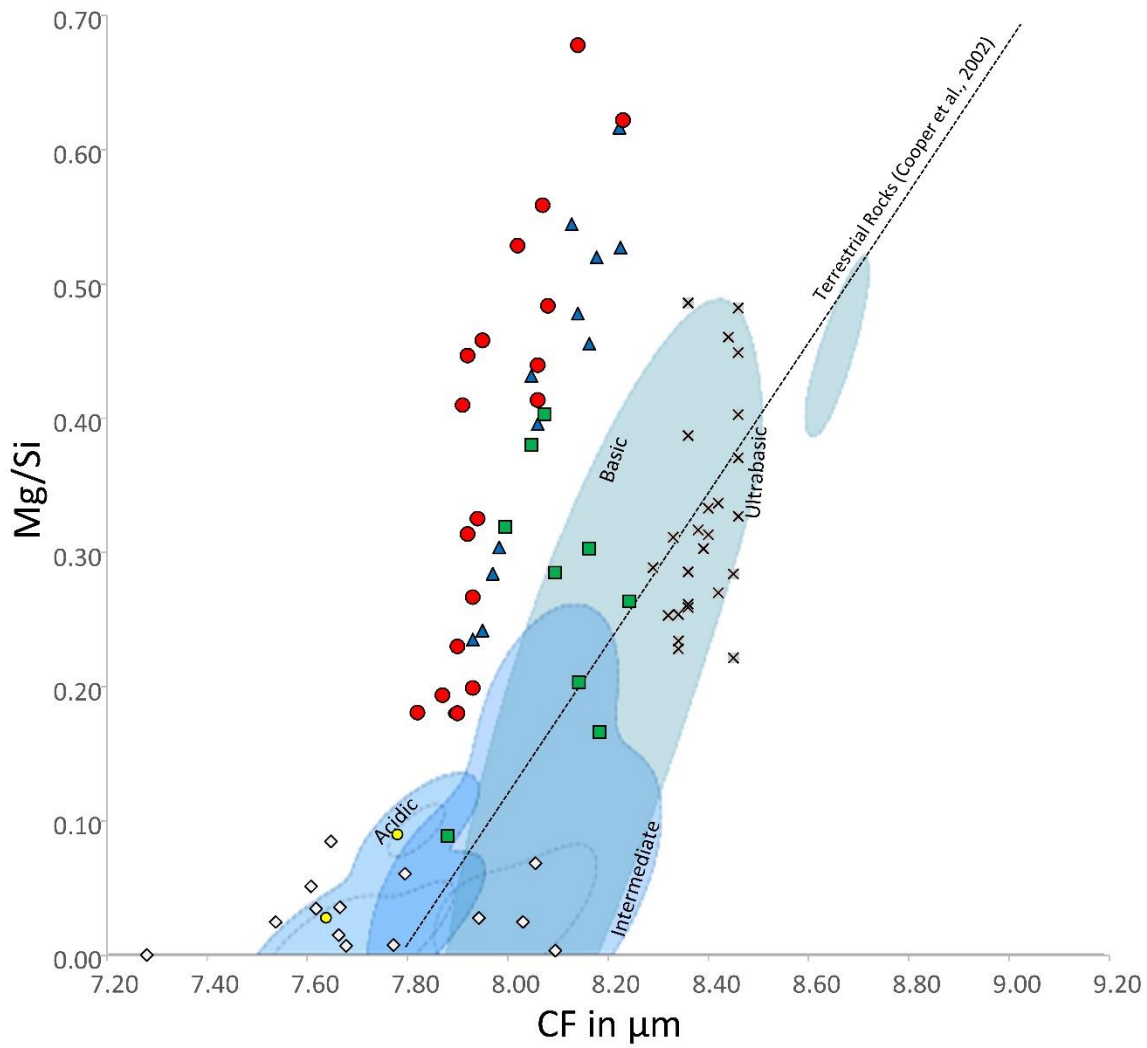
296

297

298



299 Figure 3a



- Mercury Mixtures (This study)
- Mercury Glass Component (Morlok et al., 2021)
- ▲ Bulk Synthetic Mercury Glasses (Morlok et al., 2017, 2020a)
- △ Micro Synthetic Mercury Glasses (Morlok et al., 2017, 2020a)
- Bulk Synthetic Planetary Glasses (Morlok et al., 2020a)
- Micro Synthetic Planetary Glasses (Morlok et al., 2020a)
- ◇ Impact Rocks and Glasses (Morlok et al., 2016a and b)
- × Glass Basalt Evaporation Experiments (Morlok et al., 2020b)

300 Figure 3b

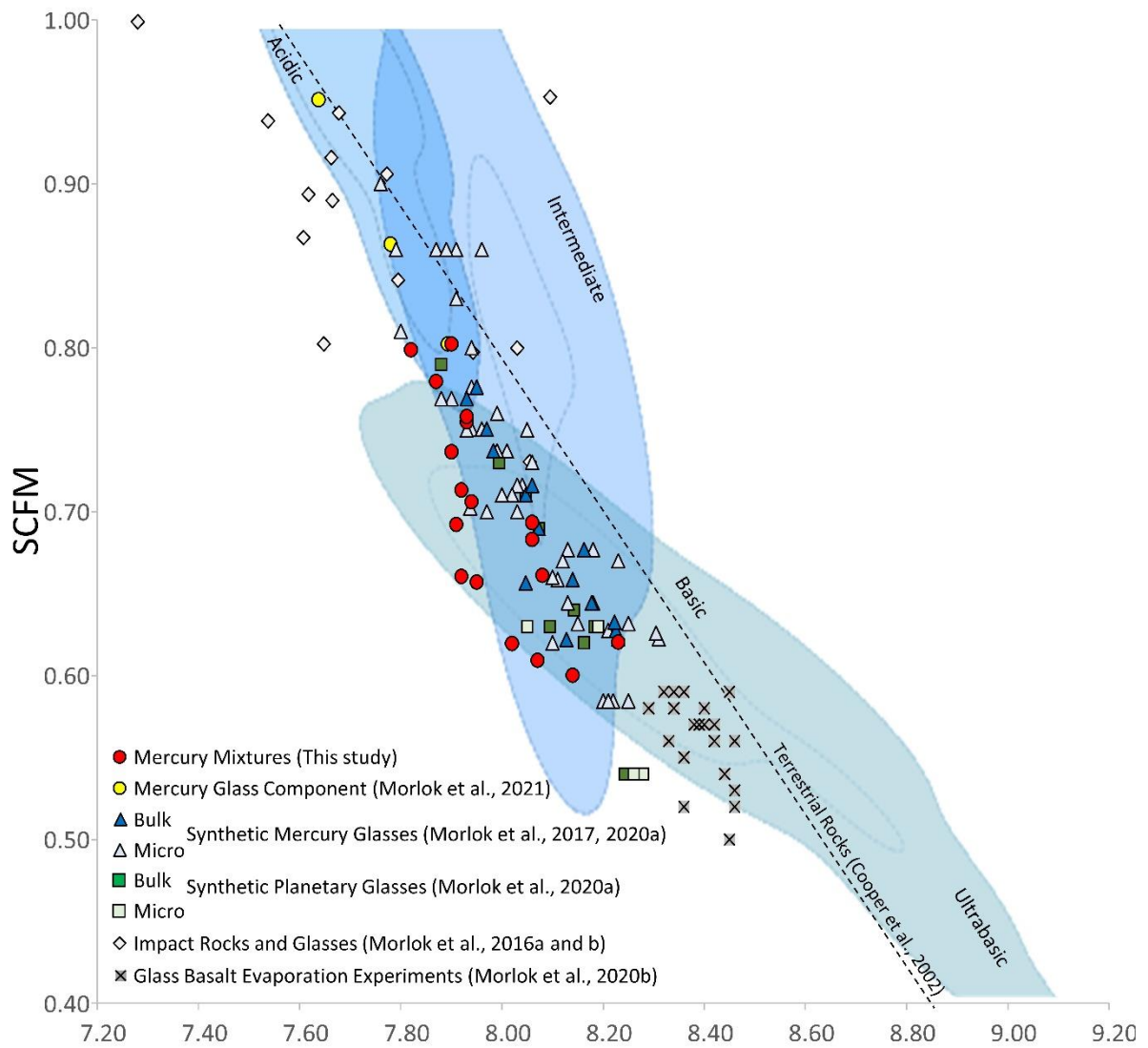


Figure 3c

302 **Figure 3. (a)** Correlation of SiO₂ abundance with CF position. Results from this study (red circles) mainly
303 fall into the intermediate area. **(b)** Comparison of the Mg/Si ratio with the CF. The refractory glasses
304 produced with laser-heating (Morlok et al., 2020b) is easy to distinguish from the samples with hermean
305 and planetary compositions. **(c)** Comparison of SCFM (SiO₂, CaO, FeO, MgO) index of polymerization to
306 CF position. Blue shaded areas and dashed line mark are from Cooper et al. (2002) for terrestrial rocks.
307

308 **4.2 Correlation of Bulk Composition with Spectral Parameters**

309 **Christiansen Feature and SiO₂**

310 The CF can be extracted even from 'noisy' spectra. Hence any correlation of the CF with other features
311 will help to derive basic information about composition and mineralogy from remote sensing data. A
312 classical method to correlate the average CF of all grain size fractions with chemical composition is the
313 comparison of the SiO₂ content (wt.%) with the CF (Cooper et al., 2002). The comparison of the hermean
314 mixtures in this study with earlier results (Fig.3a) shows that most of the mixtures fall close to the
315 correlation line for terrestrial materials, which is the best fit for results of a range of terrestrial rocks
316 scattering a bit due to compositional variances as indicated by the blue shaded areas (Cooper et al.,
317 2002). Furthermore, the results fall into or very close to the field for intermediate rocks.
318

319 **Christiansen Feature and Bulk Mg/Si**

320 Absolute element abundances are difficult to determine from mid-IR remote sensing data. Hence, we
321 use the element ratio between Mg and Si for a correlation with the CF, as ratios of chemical data of two
322 major elements is easier to extract from the space probe data (Fig.3b). In combination with the CF it
323 provides a set of parameters relatively easily extracted from remote sensing data.
324 Here, our results fall along the area of synthetic Mercury composition glasses (Morlok et al., 2017a,
325 2020a). The terrestrial impact glasses and the refractory glass from laser-heated melting experiments
326 (Morlok et al., 2020b) are clearly in a separate field compared to our samples relevant to Mercury. This

327 separation could help to identify glassy material formed in high-velocity impacts from such produced in
328 volcanic processes.

329

330 **Christiansen Feature and SCFM**

331 The SCFM index expresses the degree of polymerization based on the $\text{SiO}_2/\text{SiO}_2+\text{CaO}+\text{FeO}+\text{MgO}$ relation
332 (Salisbury and Walter, 1989). Similar to earlier studies, most of the results plot systematically below the
333 terrestrial correlation line (Fig.4c). This could be related to the varying degrees of polymerization of the
334 mixtures, however the correlation between glass content and SCFM is very weak ($R^2=0.04$) The results
335 show similarities to the intermediate, basic and basaltic terrestrial rocks (Cooper et al., 2002)

336

337 **4.3. Comparison with Remote Sensing Data of Mercury**

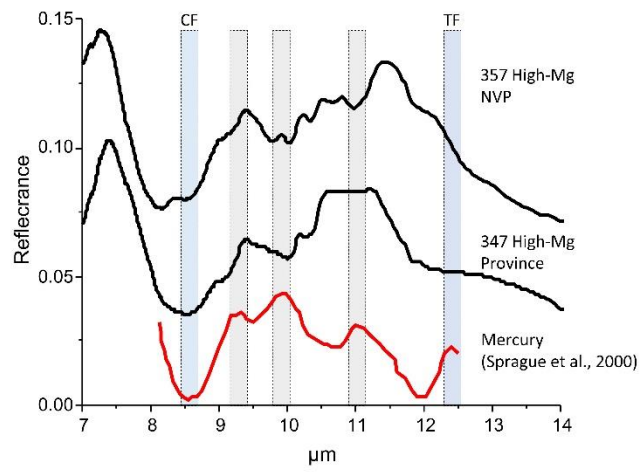
338 Only few mid-infrared spectra are so far available for Mercury. Owing to technical reasons they cover
339 larger surface regions (10^4 – 10^6 km²) and offer only weak spectral contrast and low signal to noise ratios
340 (Sprague et al., 2007). Therefore, we only use as an example the spectrum with the highest signal to
341 noise for our comparisons. The spectrum integrates a region at about 210–250° longitude and was
342 obtained by the Mid Infrared Camera (MIRAC) at the Kitty Peak Observatory (Sprague et al., 2000).

343 The spectrum recalculated from emission (Fig.4) shows a CF at 8.5 μm , three strong RBs at 9.3 $^\circ\mu\text{m}$,
344 9.9 $^\circ\mu\text{m}$, and 11 $^\circ\mu\text{m}$. A potential TF is visible at 12.4 $^\circ\mu\text{m}$. We compare it with our results of the 0-25 μm
345 fraction of two mixtures reproducing some of the features.

346 The olivine-rich 347 High-Mg Province mixture reproduces the CF of the hermean spectrum, and also has
347 an RB at 9.4 μm , near the 9.3 μm feature of the surface spectrum. A broad feature at 11 $^\circ\mu\text{m}$ overlaps
348 with a (much narrower) band of the surface spectrum at the same position.

349 Plagioclase and enstatite-rich 357 High-Mg NVP mixture has a low-point at 8.5 μm , a strong RB at 9.4 $^\circ\mu\text{m}$
350 and a minor RB at 9.9 $^\circ\mu\text{m}$. These features are similar to the CF at 8.5 μm and the second and third RB
351 (9.3 $^\circ\mu\text{m}$ and 9.9 $^\circ\mu\text{m}$) of the hermean sample.

352



354 **Figure 4.** Comparison of Plagioclase and enstatite-rich 357 High-Mg NVP, and olivine-rich 347 High-Mg
355 Province mixtures with a Mercury surface spectrum (recalculated from emissivity) (Sprague et al., 2000,
356 2007). Shaded areas mark characteristic features of the hermean spectrum.

357

358 **5. Summary & Conclusions**

359 We mixed bulk grain size fractions of analog materials relevant to the distinct terranes of Mercury. The
360 powdered samples were analyzed in diffuse reflectance in the mid-infrared (2 μm – 20 μm).

361 The resulting spectra can be divided into three groups: (1) such as dominated by a single glass feature,
362 (2) a group with forsterite, and (3) a group dominated by pyroxene bands. Plagioclase features, even
363 when the phase is dominating the composition, are usually ‘overprinted’ by forsterite and pyroxene
364 bands.

365 The spectral parameter CF in comparison with chemistry (SiO_2) and polymerization (SCFM) places the
366 hermean mixtures mostly in the intermediate and basaltic range, similar to findings based in Peplowski
367 and Stockstill-Cahill (2019). The correlation of parameters Mg/Si ratio and CF, that are easily obtainable
368 in remote sensing, allows to distinguish materials that were formed by high energy evaporation
369 processes in impacts from those formed by melting processes.

370 Preliminary comparison with a high-quality spectrum of the hermean surface (Sprague et al., 2000) show
371 some similarity with band positions of IcP-HCT and High-Mg NVP mixtures, but none of our spectra is
372 able to reproduce the remote sensing data entirely. This is not unexpected since further conditions (e.g.
373 temperature) will also affect spectral properties, and this will have to be addressed by future studies.

374

375

376

377

378 **Acknowledgements**

379 A.M., M.P.R., A.N.S., I.W. and H.H. are supported by the DLR grant 50QW1701 and 50QW2201A1302. BC
380 is a Research Associate of the Belgian Fund for Scientific Research-FNRS.

381

382

383 **References**

384 Cartier, C., Wood, B.J. (2019) The Role of Reducing Conditions in Building Mercury. *Elements* 15, 39-45.

385 Charlier, B., Grove, T.L., Zuber, M.T. (2013) Phase equilibria of ultramafic compositions on mercury and
386 the origin of the compositional dichotomy. *Earth Planet. Sci. Lett.* 363, 50–60

387 Christensen, P.R., Bandfield, J.L., Hamilton, V.E. (2001) Mars global surveyor thermal emission
388 spectrometer experiment: investigation description and surface science results. *J. Geophys. Res.* 106
389 (E10), 23823–23872.

390 Cooper, B.L., Salisbury, J.W., Killen, R.M., Potter, A.E. (2002) Midinfrared spectral features of rocks and
391 their powders. *J. Geophys. Res.* 107 (E4), 5017–5

392 Daly, T., Gavin, P., Chevrier, V. (2011) Effects of Thermal Alteration on the Near-Infrared and Mid-
393 Infrared Spectra of Martian Phyllosilicates. 42nd Lunar and Planetary Science Conference, LPI
394 Contribution No. 1608, p.1164

395 Denevi, B.W., Ernst, C.M., Prockter, L.M., Robinson, M. S. (2020) The Geologic History of Mercury.
396 In:Salomon, Nittler, Anderson (Eds.) *Mercury – The View after Messenger*. Cambridge.

397 Donaldson Hanna, K. L., Greenhagen, B. T., Patterson, W. R., Pieters, C. M., Mustard, J. F., Bowles, N. E.,
398 Paige, D. A., Glotch, T. D., Thompson, C., Emery, J.P., Sprague, A.L., Witteborn, F.C., Colwell, F.C. (2007)
399 Effects of varying environmental conditions on emissivity spectra of bulk lunar soils: Application to
400 Diviner thermal infrared observations of the Moon. *Icarus* 283, 326-342.

401 Hapke, B. (1993) Theory of Reflectance and Emittance Spectroscopy. Cambridge Univ, Press, New York.

402 Hiesinger H., Helbert J., Mertis Co-I Team (2010) The Mercury Radiometer and Thermal Infrared
403 Spectrometer (MERTIS) for the BepiColombo mission. Planetary and Space Science 58, 144–165.

404 Hiesinger H, Helbert J, Alemanno G, Bauch KE, D'Amore M, Maturilli A, Morlok A, Reitze MP, Stangarone
405 C, Stojic AN, Varatharajan I, Weber I, the MC-IT (2020) Studying the Composition and Mineralogy of the
406 Hermean Surface with the Mercury Radiometer and Thermal Infrared Spectrometer (MERTIS) for the
407 BepiColombo Mission: An Update. Space Sci Rev 216(6):110 doi:10.1007/s11214-020-00732-4

408 Izenberg, N. R. et al. The low-iron, reduced surface of Mercury as seen in spectral reflectance by
409 MESSENGER. Icarus 228, 364–374 (2014).

410 McCubbin FM, Riner MA, Vander Kaaden KE, Burkemper LK (2012) Is Mercury a volatile-rich planet?
411 Geophysical Research Letters 39:L09202 doi:10.1029/2012GL051711

412 Van der Meer, F. (1995) Estimating and simulating the degree of serpentinization of peridotites using
413 hyperspectral remotely sensed imagery. Nonrenewable Resources 4, 84-98.

414 Morlok, A., Stojic, A., Dittmar, I., Hiesinger, H., Tiedeken, M., Sohn, M., Weber, I., Helbert, J. (2016a) Mid-
415 infrared spectroscopy of impactites from the Nördlinger Ries impact crater. Icarus 264, 352–368.

416 Morlok, A., Stojic, A., Weber, I., Hiesinger, H., Zanetti, M., Helbert, J. (2016b) Mid-infrared bi-directional
417 reflectance spectroscopy of impact melt glasses and tektites. Icarus 278, 162–179.

418 Morlok, A., Klemme, S., Weber, I., Stojic, A., Sohn, M., Hiesinger, H. (2017a) IR spectroscopy of synthetic
419 glasses with mercury surface composition: analogs for remote sensing. Icarus 296, 123–138.

420 Morlok, A., Klemme, S., Weber Iris. Stojic A., Sohn M., Hiesinger H., Helbert, J. (2020a) Mid-infrared
421 spectroscopy of planetary analogs: A database for planetary remote sensing. Icarus 324, 86–103.

422 Morlok, A., Hamann, C., Martin, D., Weber, I., Joy, K.H., Hiesinger, H., Wogelius, R., Stojic, A.N., Helbert, J.
423 (2020b) Mid-infrared spectroscopy of laser-produced basalt melts for remote sensing application. *Icarus*
424 335, 113410.

425 Morlok, A., Renggli, C., Charlier, B., Reitze, M. P., Klemme, S., Namur, O., Sohn, M. Martin, D., Weber, I.,
426 Stojic, A. N., Hiesinger, H., Joy, K. H., Wogelius, R., Tollan, P., Carli, C., Bauch, K. E., Helbert, J. (2021) Mid-
427 infrared reflectance spectroscopy of synthetic glass analogs for Mercury surface studies. *Icarus* 361,
428 114363.

429 Mustard, J.F., Hays, J.E. (1997) Effects of hyperfine particles on reflectance spectra from 0.3 to 25 μm .
430 *Icarus* 125, 145–163.

431 Namur, O., Charlier, B. (2017) Silicate mineralogy at the surface of mercury. *Nat. Geosci.* 10, 9–13.

432 Namur O, Collinet M, Charlier B, Grove TL, Holtz F, McCammon C (2016a) Melting processes and mantle
433 sources of lavas on Mercury. *Earth and Planetary Science Letters* 439:117-128

434 Namur O, Charlier B, Holtz F, Cartier C, McCammon C (2016b) Sulfur solubility in reduced mafic silicate
435 melts: Implications for the speciation and distribution of sulfur on Mercury. *Earth and Planetary Science*
436 *Letters* 448:102-11

437 Neumann, G. A. (2013) Bright and dark polar deposits on Mercury: Evidence for surface volatiles. *Science*
438 339, 296–300.

439 Nicodemus, F.E. (1965) Directional reflectance and emissivity of an opaque surface. *Appl. Opt.* 4, 767.

440 Nittler, L.R., Starr, R.D., Weider, S.Z., McCoy, T.J., Boynton, W.V., Ebel, D.S., Ernst, C.M., Evans, L.G.,
441 Goldsten, J.O., Hamara, D.K. (2011) The major-element composition of Mercury's surface from
442 MESSENGER X-ray spectrometry. *Science* 333,1847–1849.

443 Nittler LR, Frank EA, Weider SZ, Crapster-Pregont E, Vorburger A, Starr RD, Solomon SC (2020) Global
444 major-element maps of Mercury from four years of MESSENGER X-Ray Spectrometer observations.
445 *Icarus* 345:113716 doi:<https://doi.org/10.1016/j.icarus.2020.113716>

446 Peplowski PN, Lawrence DJ, Feldman WC, Goldsten JO, Bazell D, Evans LG, Head JW, Nittler LR, Solomon
447 SC, Weider SZ (2015) Geochemical terranes of Mercury's northern hemisphere as revealed by
448 MESSENGER neutron measurements. *Icarus* 253:346-363
449 doi:<http://dx.doi.org/10.1016/j.icarus.2015.02.002>

450 Peplowski PN, Evans LG, Hauck SA, McCoy TJ, Boynton WV, Gillis-Davis JJ, Ebel DS, Goldsten JO, Hamara
451 DK, Lawrence DJ, McNutt RL, Nittler LR, Solomon SC, Rhodes EA, Sprague AL, Starr RD, Stockstill-Cahill KR
452 (2011) Radioactive elements on Mercury's surface from MESSENGER: Implications for the planet's
453 formation and evolution. *Science* 333(6051):1850-1852 doi:10.1126/science.1211576

454 Peplowski, P.N., Stockstill-Cahill, K. (2019) Analytical identification and characterization of the major
455 geochemical Terranes of Mercury's northern hemisphere. *J. Geophys. Res.* 124, 2414–2429.

456 Peplowski, P. N. (2016) Remote sensing evidence for an ancient carbon-bearing crust on Mercury. *Nat.*
457 *Geosci.* 9, 273–276 .

458 Renggli, C. J., Klemme, S., Morlok, A., Berndt, J., Weber, I., Hiesinger, H., King, P. L. (2022) Sulfides and
459 hollows formed on Mercury's surface by reactions with reducing S-rich gases. *Earth and Planetary*
460 *Science Letters* 593, 117647.

461 Reitze M. P. Weber I., Morlok A., Hiesinger H., Bauch K. E., Stojic A. N., Helbert J. (2020) Mid-infrared
462 spectroscopy of crystalline plagioclase feldspar samples with various Al,Si order and implications for
463 remote sensing of Mercury and other terrestrial Solar System objects. *EPSL* 554, 116697.

464 Reitze, M. P., Weber, I., Morlok, A., Hiesinger, H., Bauch, K. E., Stojic, A. N., Helbert, J. (2021) Mid-
465 Infrared Spectroscopy of Anorthosite Samples From Near Manicouagan Crater, Canada, as Analogue for

466 Remote Sensing of Mercury and Other Terrestrial Solar System Objects. *Journal of Geophysical Research:*
467 *Planets*, 126, e06832

468 Rothery DA, Massironi M, Alemanno G, Barraud O, Besse S, Bott N, Brunetto R, Bunce E, Byrne P,
469 Capaccioni F, Capria MT, Carli C, Charlier B, Cornet T, Cremonese G, D'Amore M, De Sanctis MC,
470 Doressoundiram A, Ferranti L, Filacchione G, Galluzzi V, Giacomini L, Grande M, Guzzetta LG, Helbert J,
471 Heyner D, Hiesinger H, Hussmann H, Hyodo R, Kohout T, Kozyrev A, Litvak M, Lucchetti A, Malakhov A,
472 Malliband C, Mancinelli P, Martikainen J, Martindale A, Maturilli A, Milillo A, Mitrofanov I, Mokrousov M,
473 Morlok A, Muinonen K, Namur O, Owens A, Nittler LR, Oliveira JS, Palumbo P, Pajola M, Pegg DL, Penttilä
474 A, Politi R, Quarati F, Re C, Sanin A, Schulz R, Stangarone C, Stojic A, Tretiyakov V, Väisänen T,. (2020)
475 Rationale for BepiColombo Studies of Mercury's Surface and Composition. *Space Science Reviews* 216,
476 .66.

477 Salisbury, J.W., Walter, L.S., Vergo, N., D'Aria, D.M. (1991°) *Infrared (2,1-25 µm) Spectra of Minerals.*
478 *Johns Hopkins University Press, Baltimore, MD.*

479 Salisbury, J.W. (1993) *Mid-infrared spectroscopy: laboratory data.* In: Pieters, C.M., Englert, P.A.J. (Eds.),
480 *Remote Geochemical Analysis: Elemental and Mineralogical Composition.* Cambridge University Press.

481 Salisbury, J.W., Wald, A., Di Aria, D.M. (1994) *Thermal-infrared remote sensing and Kirchhoff's law 1.*
482 *Labaratory measurements. J. Geophys. Res.* 99 (B6), 11897–11911.

483 Salisbury, J.W., Walter, L.S. (1989) *Thermal Infrared (2.5-13.5 µm) Spectroscopic Remote Sensing of*
484 *Igneous Rock Types on Particulate Planetary Surfaces. Journal of Geophysical Research* 94, 9192-9202.

485 Sprague, A.L., Kozlowski, R.W.H., Wittebom, F.C., et al. (1994) *Mercury: evidence for anorthosite and*
486 *basalt from mid-infrared (7.5–13.5 micrometer) spectroscopy. Icarus* 109, 156–167.

487 Sprague, A., Deutsch, L.K., Hora, J., Fazio, G.G., Ludwig, B., Emery, J., Hoffmann, W.F. (2000) *Mid-infrared*
488 *(8.1–12.5 µm) imaging of Mercury. Icarus* 147, 421–432.

489 Sprague, A.L., Emery, J.P., Donaldson, K.L., Russell, R.W., Lynch, D.K., Mazuk, A.L. (2002) Mercury: mid-
490 infrared (3-13.5 μm) observations show heterogeneous composition, presence of intermediate and basic
491 soil types, and pyroxene. *Meteoritics Planet. Sci.* 37, 1255–1268.

492 Sprague, A., Warell, J., Cremonese, G., Langevin, Y., Helbert, J., Wurz, P., Veselovsky, I., Orsini, S., Milillo,
493 A. (2007) Mercury's surface composition and character as measured by ground-based observations.
494 *Space Sci. Rev.* 132, 399–431.

495 Sprague, A.L., Roush, T.L. (1998) Comparison of laboratory emission spectra with mercury telescopic
496 data. *Icarus* 133, 174–183.

497 Sprague, A. L., Donaldson Hanna, K. L., Kozlowski, R. W. H., Helbert, J., Maturilli, A., Warell, J. B., Hora, J.
498 L. (2009) Spectral emissivity measurements of Mercury's surface indicate Mg- and Ca-rich mineralogy, K-
499 spar, Na-rich plagioclase, rutile, with possible perovskite, and garnet. *Planetary and Space Science* 57,
500 364-383.

501 Stockstill-Cahill, K. R., McCoy, T. J., Nittler, L. R., Weider, S. Z., Hauck, S. A. (2012) Magnesium-rich
502 crustal compositions on Mercury: Implications for magmatism from petrologic modeling. *Journal of*
503 *Geophysical Research* 117, CiteID E00L15.

504 Vander Kaaden, K.E., McCubbin, F.M., Nittler, L.R., Peplowski, P.N., Weider, S.Z., Frank, E.A., McCoy, T.
505 (2017) Geochemistry, mineralogy, and petrology of Boninitic and Komatiitic rocks on the Mercurian
506 surface: insights into the Mercurian mantle. *Icarus*. <https://doi.org/10.1016/j.icarus.2016.11.041>. in
507 Press.

508 Vander Kaaden, K. E., McCubbin, F.M. (2016) The origin of boninites on Mercury: An experimental study
509 of the northern volcanic plains lavas. *Geochimica et Cosmochimica Acta* 173, 246-263.

510 Thomson, J.L., Salisbury, J.W. (1993) The mid-infrared reflectance of mineral mixtures (7–14 microns).
511 *Remote Sens. Environ.* 45, 1–13.

512 Vilas, F. (2016) Mineralogical indicators of Mercury's hollows composition in MESSENGER color
513 observations. *Geophys. Res. Lett.* 43, 1450–1456.

514 Weber I., Reitze M.P., Heeger M., Adolphs T., Morlok A., Stojic A.N., Hiesinger H., Arlinghaus H.F., Helbert
515 J. (2021) The effect of excimer laser irradiation on mid-IR spectra of mineral mixtures for remote sensing.
516 *EPS*: 569, 117072.

517 Weber, I.; Morlok, A.; Bischoff, A.; Hiesinger, H.; Ward, D.; Joy, K. H.; Crowther, S. A.; Jastrzebski, N. D.;
518 Gilmour, J. D.; Clay, P. L.; Wogelius, R. A.; Greenwood, R. C.; Franchi, I. A.; Münker, C. (2016)
519 Cosmochemical and spectroscopic properties of Northwest Africa 7325—A consortium study.
520 *Meteoritics & Planetary Science* 51, 3-30.

521 Weber, I., Morlok, A., Grund, T., Bauch, K. E., Hiesinger, H., Stojic, A., & Joy, K. H. (2018). A mid-infrared
522 reflectance database in preparation for space missions. In *Lunar and planetary science conference* (p.
523 1430).

524 Weider, S. Z., Nittler, L. R., Starr, R. D., Ellen, Crapster-Pregont, Peplowski, P. N., Denevi, B. W., Head, J.
525 W., Byrne, P. K., Hauck, S. A., Ebel, D. S., Solomon, S. C. (2015). Evidence for geochemical terranes on
526 mercury: global mapping of major elements with MESSENGER's X-ray spectrometer. *Earth Planet. Sci.*
527 *Lett.* 416, 109–120.

528

529

530

531

532

533

Smooth Plains	CF										
ID 343											
0-25 µm	8.04	9.01	9.63	9.92	10.20	10.54	10.82			11.65	15.69
25-63 µm	7.93		9.51	9.92	10.23	10.49	10.78		11.27		15.77
63-125 µm	7.90		9.40	9.91	10.23	10.49	10.78				15.76
125-250 µm	7.84		9.62	9.89	10.21	10.46					15.69
ID 344											
0-25 µm	7.91		9.54	9.87	10.18	10.51				11.67	14.43
25-63 µm	7.89		9.53	9.90	10.18	10.48			11.28	13.75	14.43
63-125 µm	7.84		9.51	9.89	10.20	10.48			11.30		14.47
125-250 µm	7.83		9.51	9.91	10.22	10.45	10.76	11.06	11.38	13.79	14.47
ID 345											
0-25 µm	7.97		9.59		10.16	10.56			11.42	11.75	15.81
25-63 µm	7.93		9.58		10.17	10.55					15.85
63-125 µm	7.91		9.61		10.16	10.50					15.78
125-250 µm	7.89		9.59		10.17	10.56					15.93
ID 174											
0-25 µm	7.89		9.58							11.78	
25-63 µm	7.87		9.58								
63-125 µm	7.91		9.58								
125-250 µm	7.91		9.58								
High-Mg Province											
ID 346											
0-25 µm	8.60		9.37		10.19	10.64				14.12	16.03
25-63 µm	7.91		9.37		10.19	10.57	10.79		11.21	11.92	14.84
63-125 µm	7.81		9.36		10.19	10.56	10.80			11.90	14.85
125-250 µm	7.77		9.36			10.55	10.81			12.41	14.86
ID 347											
0-25 µm	8.53		9.39		10.18	10.64	10.84				14.10
25-63 µm	8.03		9.38		10.19	10.57	10.79			11.90	15.91
63-125 µm	7.87		9.38		10.18	10.57	10.79			11.92	15.81
125-250 µm	7.83		9.37		10.18	10.56	10.79			11.92	15.81
ID 348											
0-25 µm	8.21		9.63		10.16	10.64				11.96	15.96
25-63 µm	8.14		9.56		10.16	10.59				11.92	15.94
63-125 µm	8.11		9.66		10.18	10.57				11.89	15.98
125-250 µm	8.08		9.61		10.17	10.56				11.89	15.89
ID 338											
0-25 µm	8.27			9.90						12.06	
25-63 µm	8.21			9.84							
63-125 µm	8.22			9.90							
125-250 µm	8.20			9.87							

Low-Mg NVP	CF										
ID 349											
0-25 µm	7.88		9.45		10.16	10.56			11.62	15.66	
25-63 µm	7.85		9.40		10.16	10.52				15.79	
63-125 µm	7.80		9.39		10.16	10.48				15.71	
125-250 µm	7.76		9.39		10.15	10.50				15.82	
ID 350											
0-25 µm	8.14	8.36	9.40	9.89		10.62		11.32	11.50	15.73	
25-63 µm	7.86		9.36	9.89		10.52	10.82			15.77	
63-125 µm	7.82		9.36	9.91		10.52	10.81			15.77	
125-250 µm	7.76		9.39	9.89	10.19	10.52				15.93	
ID 174											
0-25 µm	7.89		9.58						11.78		
25-63 µm	7.87		9.58								
63-125 µm	7.91		9.58								
125-250 µm	7.91		9.58								
IcP-HCT											
ID 351											
0-25 µm	8.15		9.63		10.15	10.61			11.94	16.12	
25-63 µm	8.09		9.62		10.15	10.55			11.91	15.95	
63-125 µm	8.04		9.68		10.16	10.55				15.95	
125-250 µm	8.02		9.57		10.16	10.59			11.92	15.91	
ID 352											
0-25 µm	8.14		9.54		10.16	10.64		11.30	11.90	15.92	
25-63 µm	7.87		9.48		10.16	10.58				15.91	
63-125 µm	7.83		9.44		10.16	10.55			11.91	15.91	
125-250 µm	7.79		9.39		10.16	10.55			11.90	15.91	
ID 353											
0-25 µm	8.15		9.66		10.16	10.62		11.24	11.92	16.01	
25-63 µm	7.98		9.52		10.18	10.57			11.90	15.90	
63-125 µm	7.86		9.53		10.18	10.57			11.90	15.94	
125-250 µm	7.80		9.46		10.16	10.57			11.93	15.90	
ID 354											
0-25 µm	8.18	8.34	9.46	9.93	10.18	10.72			12.14	16.01	16.47
25-63 µm	7.89		9.48		10.18	10.56			11.92	15.96	16.35
63-125 µm	7.85		9.39	9.91	10.18	10.54			11.91	15.88	16.49
125-250 µm	7.75		9.39		10.18	10.55				15.88	16.48
ID 181											
0-25 µm	8.08			9.80					11.91		
25-63 µm	8.07			9.80							
63-125 µm	8.06			9.78							
125-250 µm	8.04			9.81							

High-Mg NVP	CF												
ID 355													
0-25 μm	8.08			9.83			10.48			11.86			
25-63 μm	8.06			9.74			10.50						
63-125 μm	8.04			9.79			10.50						
125-250 μm	8.05			9.79									
ID 356													
0-25 μm	8.08		9.42	9.89	10.23	10.51	10.79		11.43		14.42		
25-63 μm	7.96		9.48	9.89	10.20	10.51			11.30		14.43	15.74	
63-125 μm	7.87		9.42	9.89	10.24	10.49					14.42	15.78	
125-250 μm	7.86		9.39	9.89		10.51	10.79				14.42	15.74	
ID 357													
0-25 μm	8.15	8.38	9.39	9.90	10.23	10.52	10.79		11.44		14.41	15.73	
25-63 μm	7.89		9.42	9.91	10.21	10.53	10.77		11.33		14.42	17.46	
63-125 μm	7.83		9.40	9.91	10.22	10.46	10.79		11.34	13.77	14.48	15.63	17.51
125-250 μm	7.81		9.37	9.91	10.21	10.49	10.79		11.34	13.77	14.48	15.70	17.54
ID 181													
0-25 μm	8.08			9.80						11.91			
25-63 μm	8.07			9.80									
63-125 μm	8.06			9.78									
125-250 μm	8.04			9.81									

Table 4. Band positions of the studied mixtures. In Bold: position of the CF of the respective grain size fractions. (In μm).

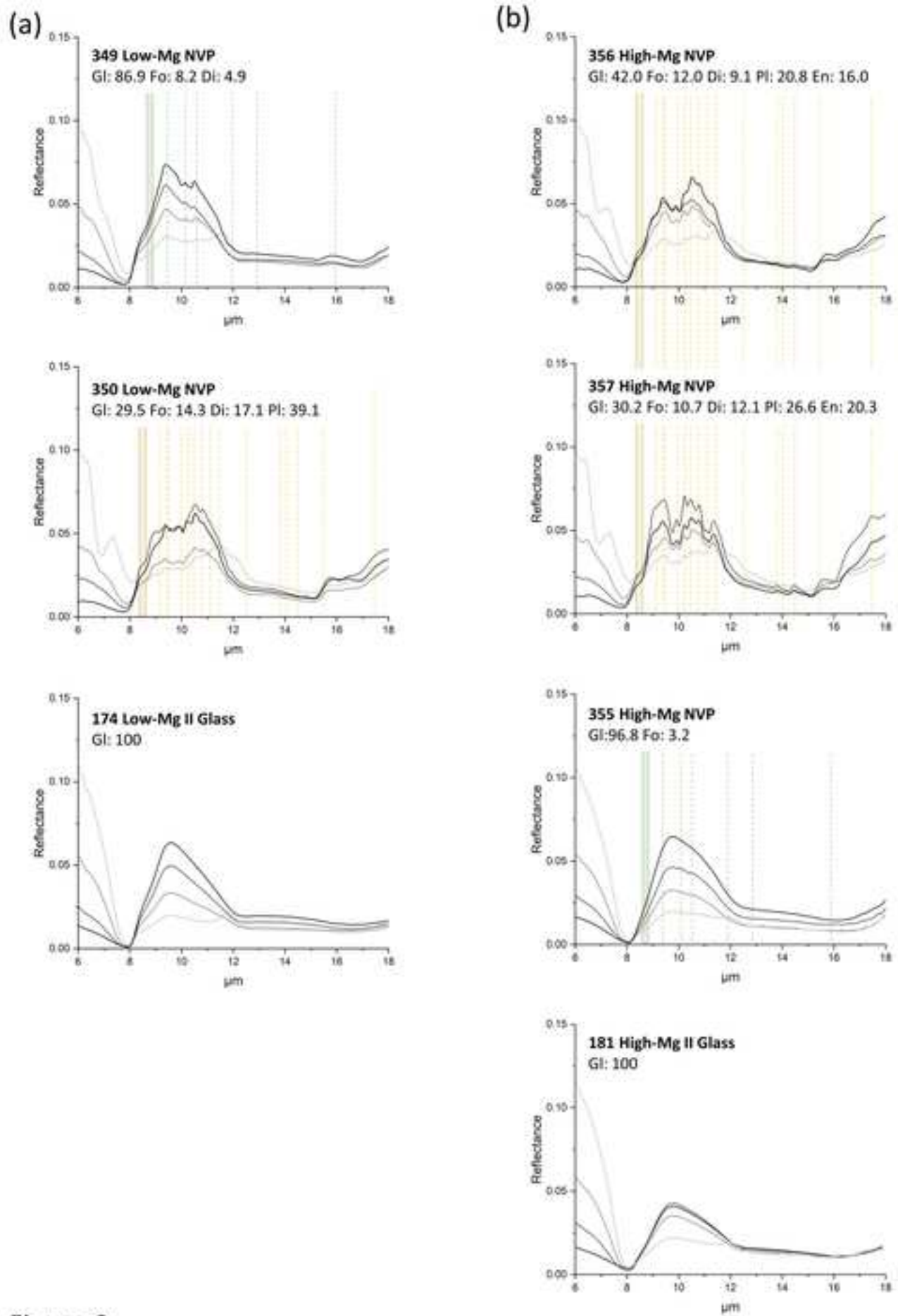


Figure 2

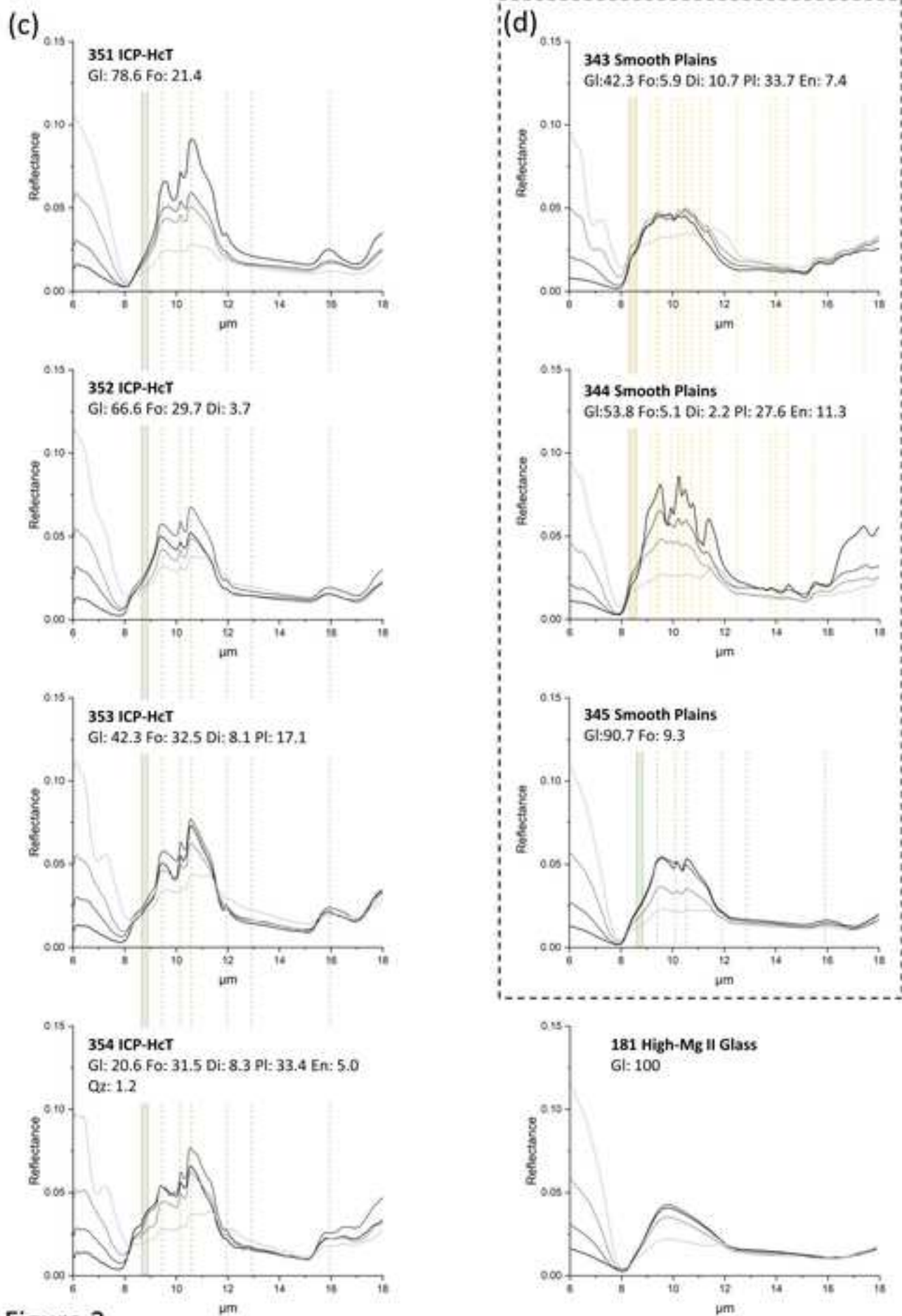


Figure 2

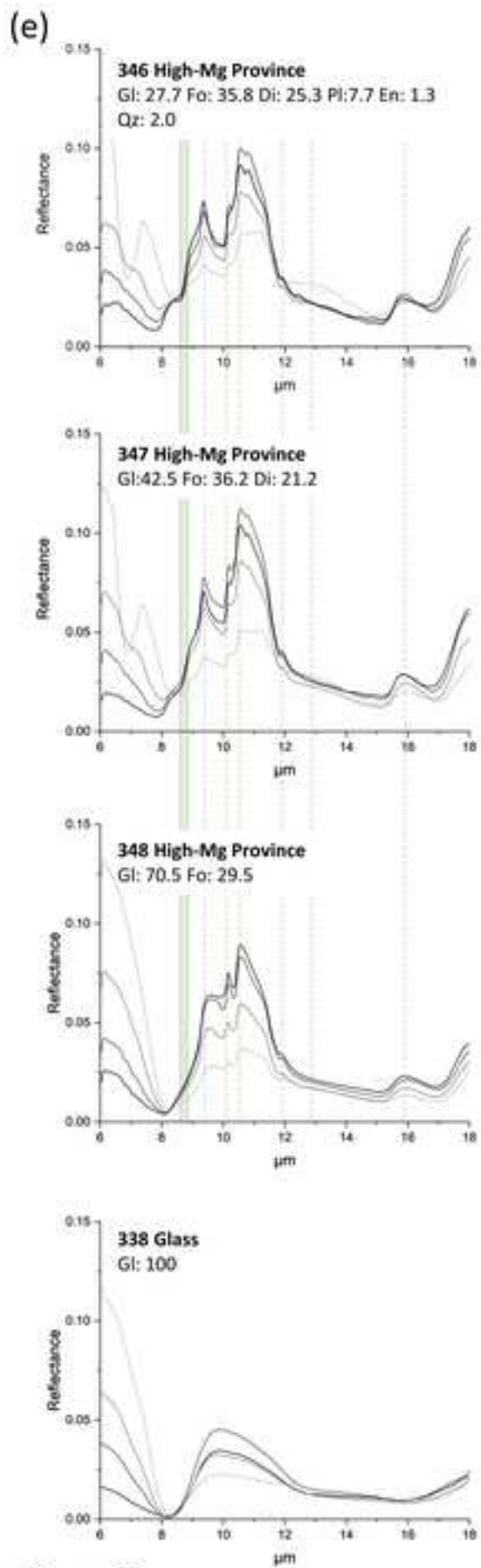


Figure 2

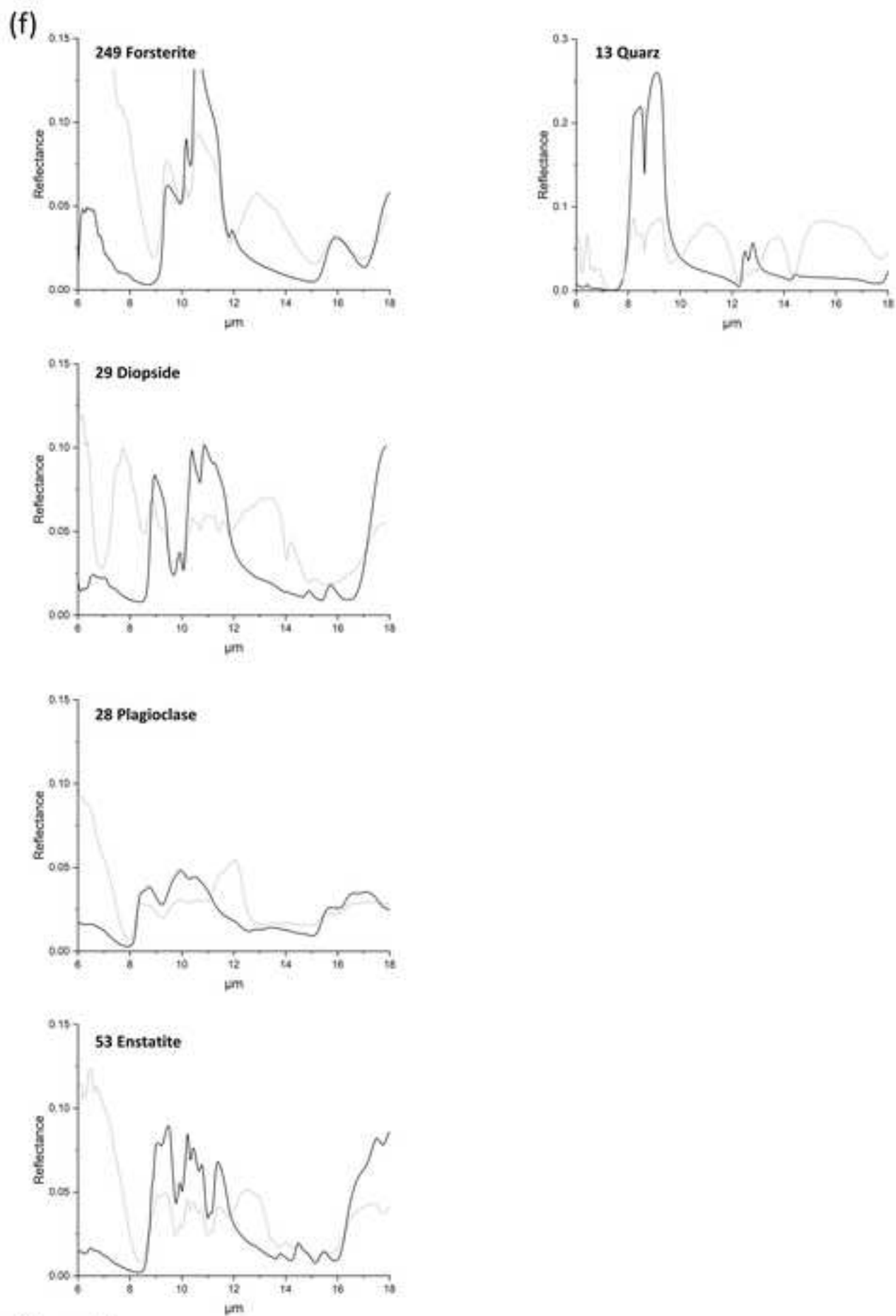


Figure 2

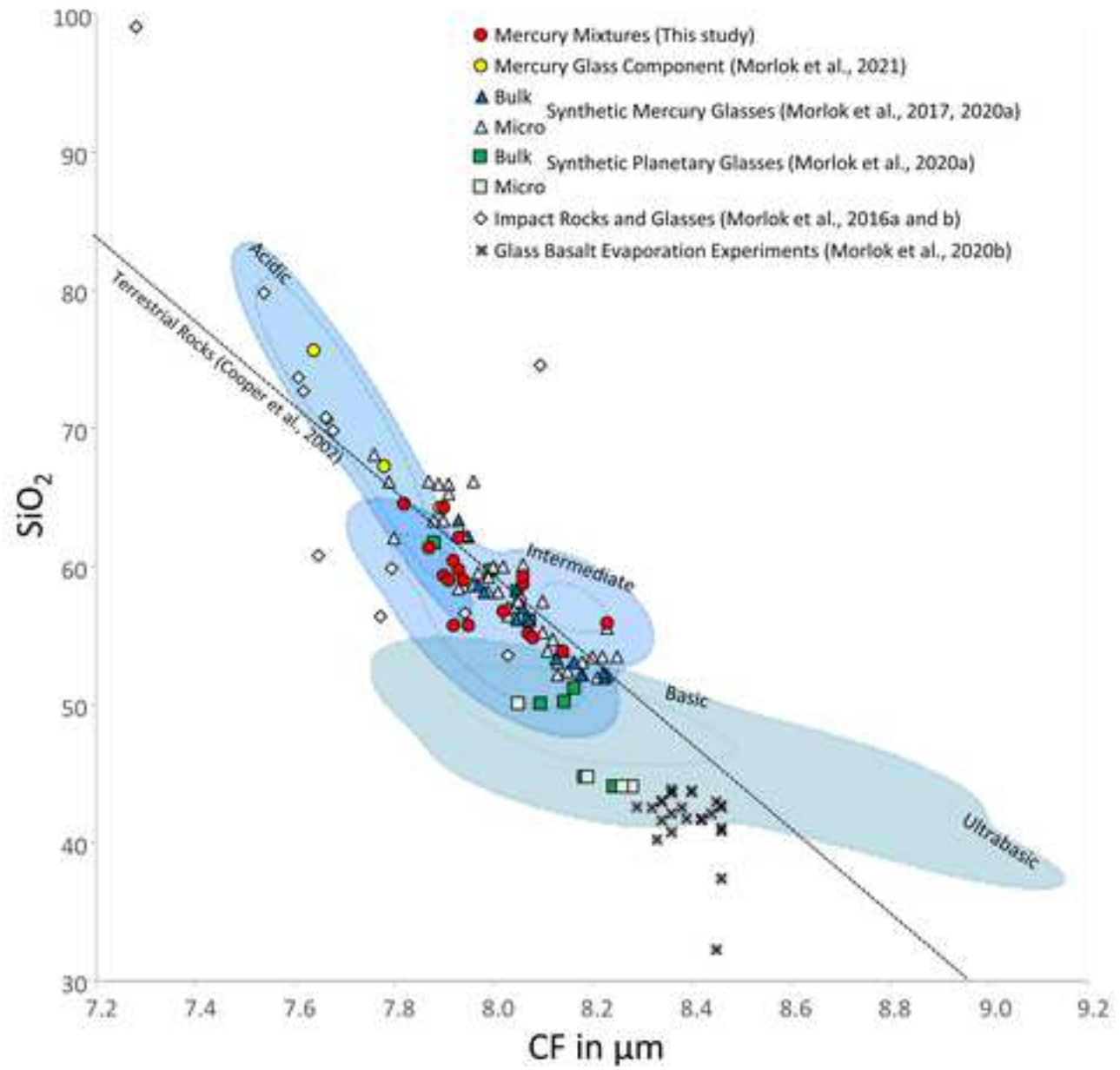
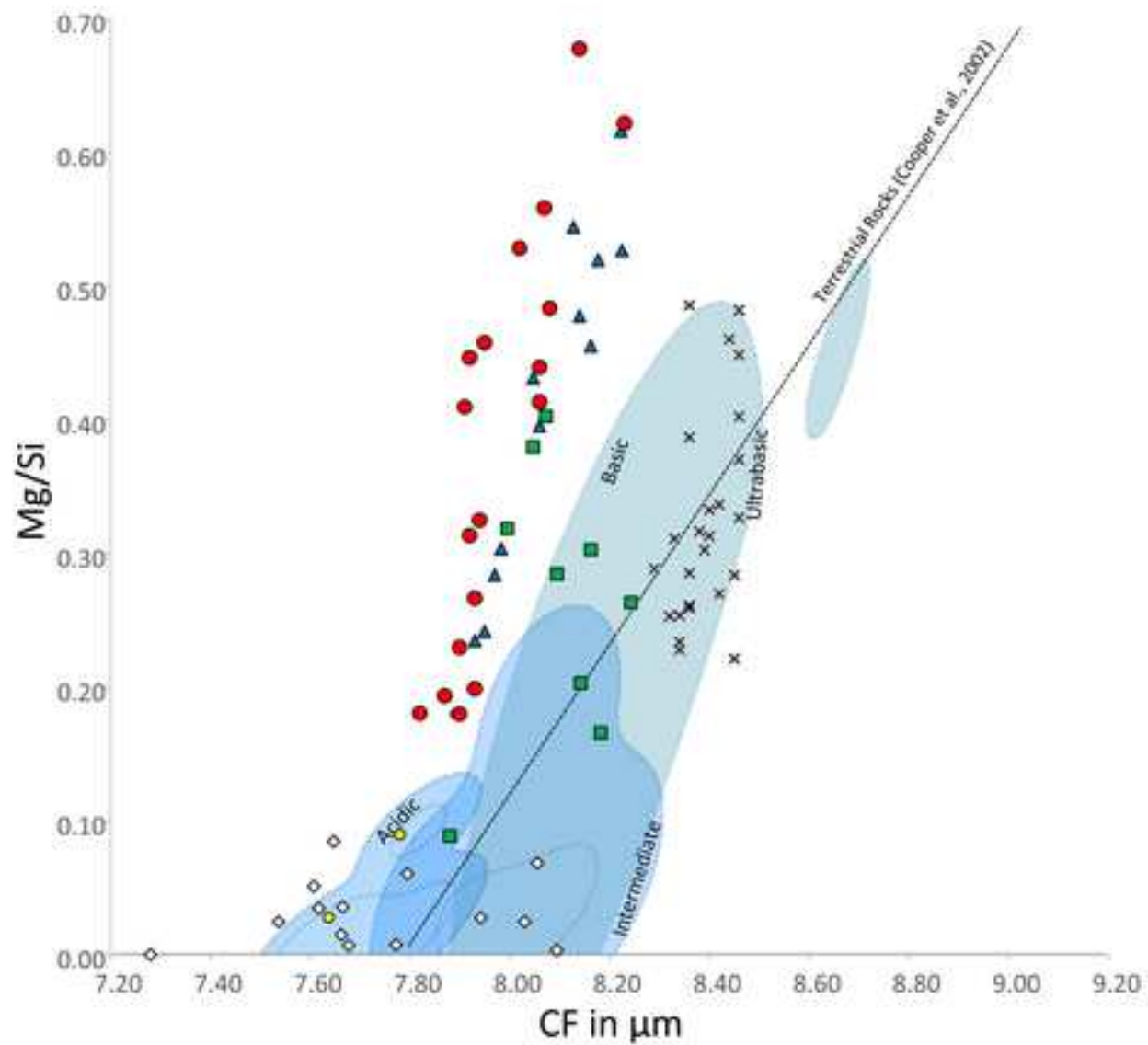


Figure 3a



- Mercury Mixtures (This study)
- Mercury Glass Component (Morlok et al., 2021)
- ▲ Bulk Synthetic Mercury Glasses (Morlok et al., 2017, 2020a)
- △ Micro Synthetic Mercury Glasses (Morlok et al., 2017, 2020a)
- Bulk Synthetic Planetary Glasses (Morlok et al., 2020a)
- Micro Synthetic Planetary Glasses (Morlok et al., 2020a)
- ◇ Impact Rocks and Glasses (Morlok et al., 2016a and b)
- × Glass Basalt Evaporation Experiments (Morlok et al., 2020b)

Figure 3b

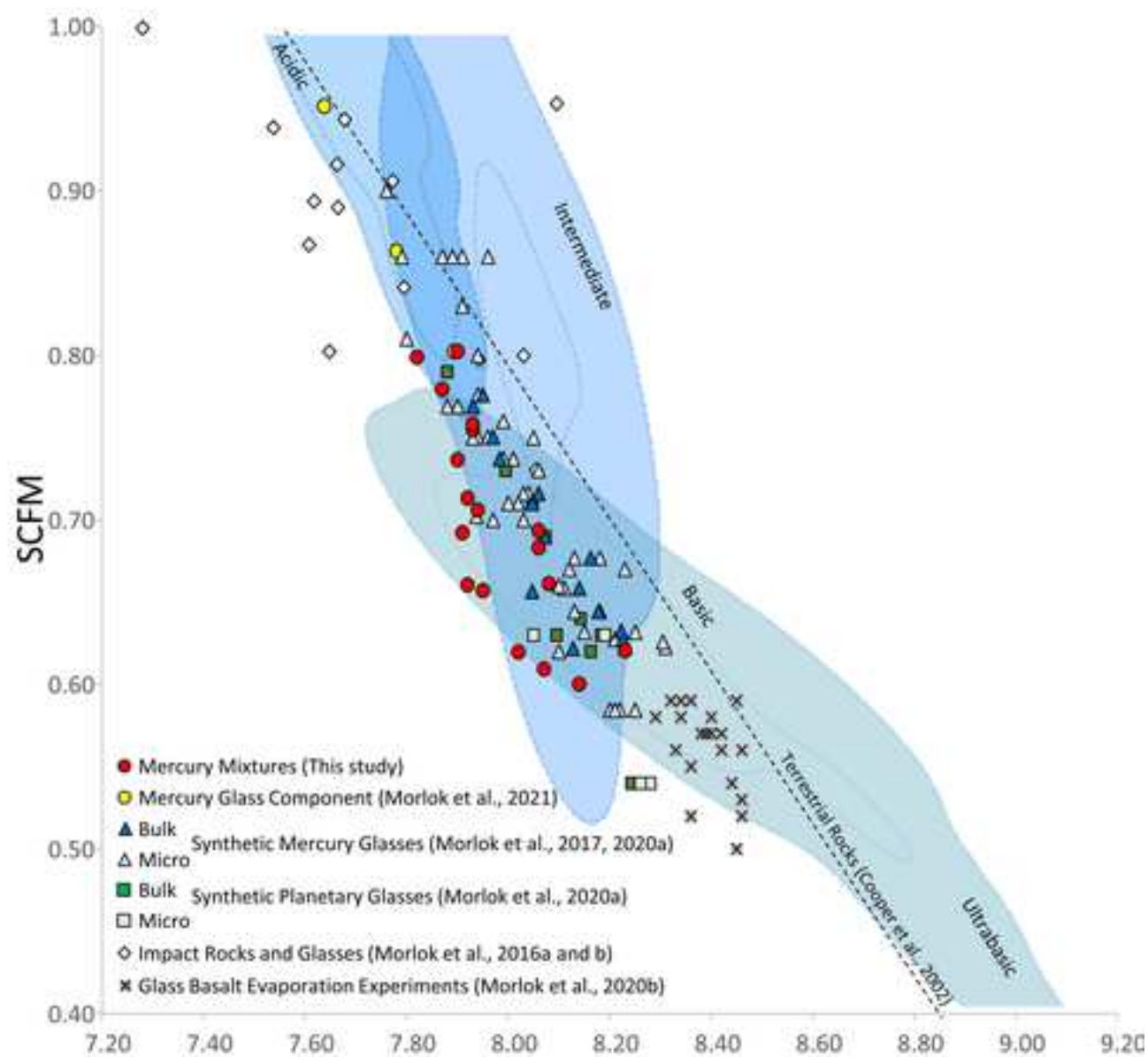


Figure 3c

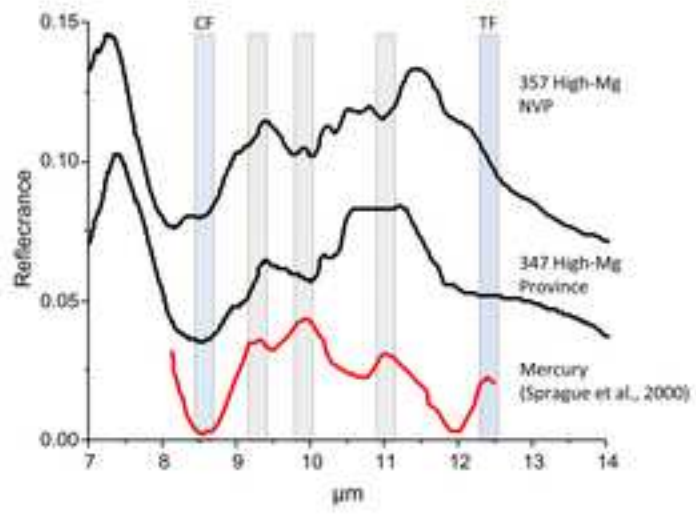
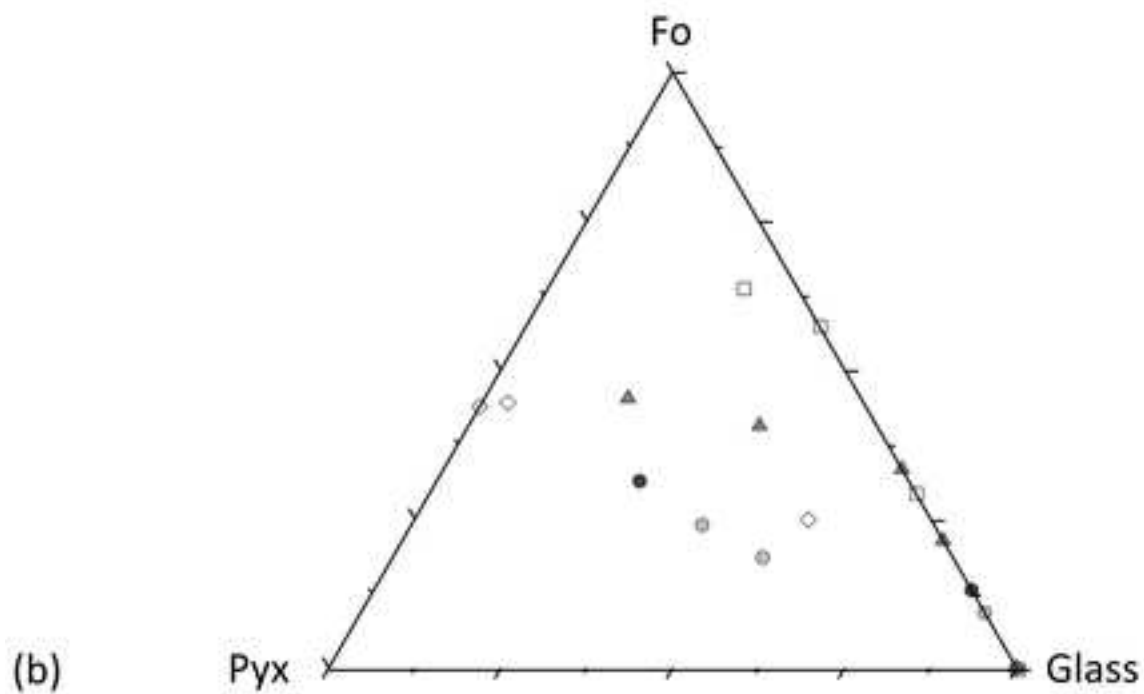
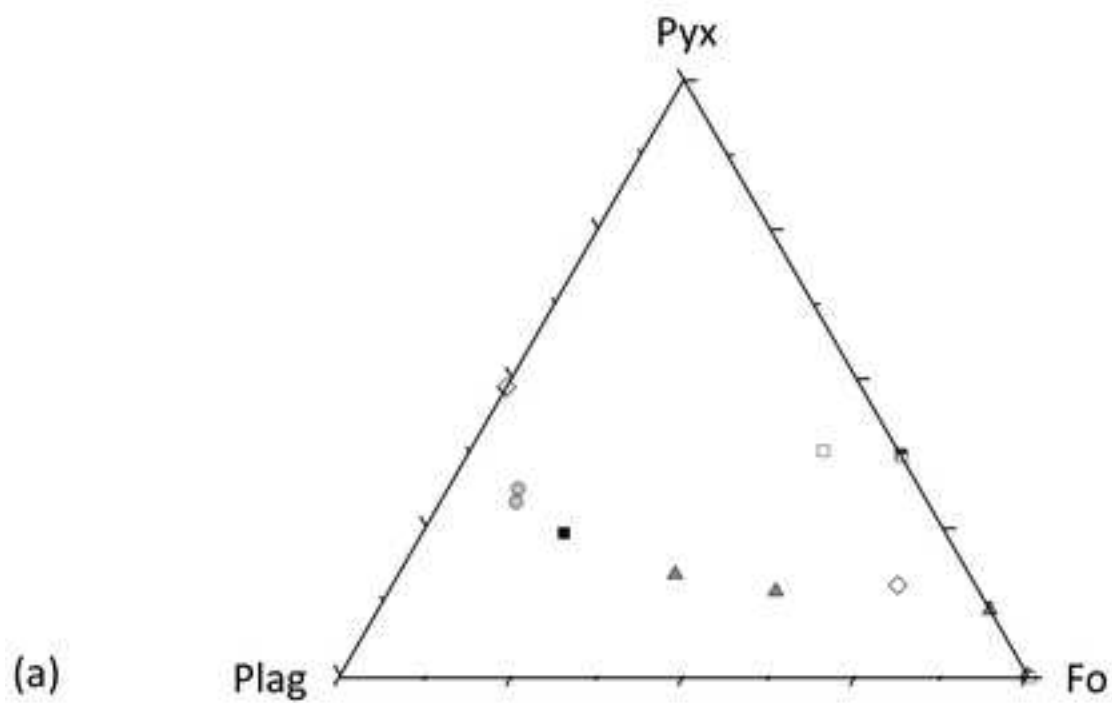


Figure 4



- Smooth Plains (SP)
- High-Magnesium Province (High-Mg Province)
- ▲ Inter-Crater Plain and Heavily Cratered Plains (ICP-HcT)
- ◇ High Magnesium Northern Volcanic Plains (High-Mg NVP)
- Low Magnesium Northern Volcanic Plains (Low-Mg NVP)

Figure 1